Chemical Geology 682 (2025) 122751

Contents lists available at ScienceDirect

Chemical Geology

journal homepage: www.elsevier.com/locate/chemgeo

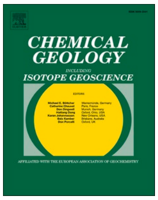

Utility of the B/Ga salinity proxy in carbonate and marly sediments

Wei Wei [a,b,c], Thomas J. Algeo [a,b,c,d], David Meyer [b], Jiangsi Liu [e], Katherine N. Snihur [f], Cody Lazowski [f], Zhiquan Li [g], Daniel S. Alessi [f], Kurt O. Konhauser [f], Yuansheng Du [a], Wenchao Yu [a,*]

[a] *State Key Laboratory of Geomicrobiology and Environmental Changes, School of Earth Science, China University of Geosciences, Wuhan 430074, China*
[b] *Department of Geosciences, University of Cincinnati, Cincinnati, OH 45221-0013, USA*
[c] *State Key Laboratory of Geological Processes and Mineral Resources, China University of Geosciences, Wuhan 430074, China*
[d] *State Key Laboratory of Oil and Gas Reservoir Geology and Exploitation, Institute of Sedimentary Geology, Chengdu University of Technology, Chengdu 610059, China*
[e] *State Key Laboratory of Isotope Geochemistry, Guangzhou Institute of Geochemistry, Chinese Academy of Sciences, Guangzhou 510640, China*
[f] *Department of Earth and Atmospheric Sciences, University of Alberta, Edmonton, Alberta, Canada*
[g] *Department of Geology, Lakehead University, Thunder Bay, Ontario P7B 7A5, Canada.*

ARTICLE INFO

Editor: Karen Johannesson

Keywords:
Boron
Gallium
Clay minerals
Brackish
Marine
Seawater chemistry

ABSTRACT

Elemental proxies are widely used for analyzing watermass salinity in ancient shale and siliciclastic mudstone formations, but their application to limestones and marls has not yet been systematically tested. Unlike the Sr/Ba and S/TOC proxies, the B/Ga proxy offers considerable, albeit untested, potential for paleosalinity determinations in carbonate-bearing facies. To evaluate this potential, we analyzed the concentrations of B and Ga, as well as those of Al, Ca, and other lithology-associated elements, in a large suite of modern and ancient marine and marine-influenced carbonate samples, including both sediments and fossils. Our results show that B/Ga ratios tend to be elevated in carbonate-rich material due to low concentrations of Ga, which is primarily present in the detrital siliciclastic fraction. In marly sediments, robust salinity facies determinations are generally possible for samples with Ga concentrations as low as 3 ppm, compared to the typical range of 15–20 ppm in shales. For carbonate samples with Ga concentrations <3 ppm, reliable salinity facies estimates may still be obtained using excess boron (B_{xs}) present in the sample, calculated as $B_{total} - 6 \times Ga$. Excess boron content is typically ~10–20 ppm for carbonates from fully marine facies. Deviations from this range may signal watermass salinities that are lower or higher than the normal marine salinity range of ~33–38 psu (practical salinity units). This study establishes, for the first time, a robust framework for evaluating depositional salinities in ancient marine and marine-influenced carbonate and marl formations, providing a valuable tool for future paleoenvironmental research.

1. Introduction

Since Wei et al. (2018) and Wei and Algeo (2020) demonstrated the utility of elemental proxies such as B/Ga, Sr/Ba and S/TOC for reconstructing watermass salinity in ancient shale and siliciclastic mudstone formations, salinity reconstruction has garnered significant attention in paleoenvironmental research. These proxies have proven highly effective in resolving a wide range of scientific problems. First, documenting secular variation in salinity provides critical insights into the hydrographic history and paleoenvironmental evolution of epicontinental seas and marginal marine basins (e.g., Remírez and Algeo, 2020; Wei et al., 2022; Liu et al., 2024a, 2024b; Remírez et al., 2024; Wang et al., 2024). Second, salinity and water-column stratification significantly influence watermass properties such as redox conditions and productivity, making salinity reconstruction in ancient depositional systems essential for understanding the factors controlling these properties (e.g., Cheng et al., 2021, 2023; Gilleaudeau et al., 2021, 2023; Song et al., 2021; Yu et al., 2022; Wei et al., 2024; Remírez et al., 2025). Third, a more comprehensive understanding of the covariation between salinity and redox conditions in the water column can aid in explaining paleoecological changes within a paleoenvironmental system (e.g., Song et al., 2021).

The salinity facies thresholds of these elemental proxies, such as B/Ga, Sr/Ba, and S/TOC, were established using modern argillaceous sediments, with the intention of applying these thresholds to ancient

---

* Corresponding author.
E-mail address: yuwenchaocug@163.com (W. Yu).

https://doi.org/10.1016/j.chemgeo.2025.122751
Received 17 January 2025; Received in revised form 16 March 2025; Accepted 18 March 2025

shale and mudstone formations (Wei et al., 2018; Wei and Algeo, 2020). (Note that these proxies are applicable only to marine facies, brackish facies with marine influence such as estuaries and coastal lagoons, and freshwater continental facies; they cannot be assumed valid for saline lakes, because every lake system has a unique watermass chemistry that may have a B/salinity relationship unlike that of the ocean.) The theoretical basis for the B/Ga and Sr/Ba proxies in argillaceous facies lies in their adsorption of aqueous ionic species of B and Sr onto clay minerals in sediments, proportional to their concentrations in the overlying water column. Thus, a suitable substrate for ionic species uptake is essential, effectively precluding the use of these proxies in sandstone, conglomerate, and chert facies. The situation is more complex for carbonates, which can incorporate ionic species directly into their mineral lattices in proportion to the concentrations of those species in the surrounding fluid medium (Rimstidt et al., 1998; Smrzka et al., 2019). However, the Sr/Ba proxy is generally invalid for salinity analysis of carbonates due to the presence of excess Sr derived from carbonate minerals, and the S/TOC proxy is of limited use because most carbonate sediments have low organic content (Wei and Algeo, 2020). In contrast, there is no inherent limitation that would prevent the B/Ga ratio from serving as an effective salinity proxy in carbonate-rich facies, making it a promising avenue for further investigation.

Carbonates are the second most abundant type of sediment and sedimentary rock, comprising ~20–25 % of the crustal sedimentary reservoir (Boggs, 2006). For this reason, it would be useful to have an elemental proxy for reconstruction of salinity facies in ancient carbonate depositional systems. To date, B/Ga values have been reported for a limited number of carbonate-bearing samples in the context of studies focused mainly on shales, e.g., the Mn-carbonates of the Cryogenian Datangpo Formation (Fm) (Cheng et al., 2021; Wei et al., 2024) and various carbonate-bearing sediments of Pennsylvanian (Wei et al., 2022), Permian (Xia et al., 2020), and Paleogene age (Wei et al., 2018). In many of these units, B/Ga values for carbonate-rich samples produce paleosalinity signals similar to those of coeval shale samples, though exceptions have been noted. However, the validity of the B/Ga proxy for salinity analysis in ancient carbonate facies has not been systematically evaluated. In particular, it remains unclear whether the salinity facies thresholds developed for argillaceous sediments (Wei and Algeo, 2020) can be directly applied to carbonates and marls.

This study investigates carbonate-rich samples spanning a range of ages to assess the validity of B/Ga as a salinity proxy in carbonate-rich facies. Specifically, we analyzed four sets of carbonate samples for B, Ga, and other elements: (1) modern marine carbonate shells and skeletal sediments and ancient marine carbonate fossils ($n = 45$); (2) Cretaceous deep-ocean sediments (limestones and shales) from IODP Sites 1138 A (Kerguelen Plateau), 1210B (Shatsky Rise), and 1258 A (Demerara Rise) ($n = 24$), (3) Upper Pennsylvanian epeiric sea sediments (limestones, marls and shales) from the North American Illinois Basin and Midcontinent Shelf ($n = 343$), and (4) Upper Devonian limestones of the Westerdale Member of the Lower Ireton Fm and black shales of the Duvernay Fm from the restricted-marine Alberta Basin in western Canada ($n = 43$). Note that some shales were included in sample suites (2) to (4) for the purpose of comparing their B/Ga signals to those of the carbonate-rich samples. Note that, throughout this study, we make use of the following operational definitions: “limestone” (Al < 0.5 %), “argillaceous limestone” (Al = 0.5–2 %), “marl” (Al = 2–6 %), and “shale” (Al >6 %). As shown below, the distinction between limestone (Al < 2 %) and marl-shale (Al >2 %) is particularly important because it is the threshold below which B/Ga becomes unsuitable for use as a paleosalinity proxy.

2. Geological settings and materials

2.1. Modern and ancient skeletal carbonates

All (sub-)Recent ($n = 28$) and ancient ($n = 17$) skeletal samples used in this study (Table S1) were collected in the field over the past 50 years and curated in the University of Cincinnati Department of Geosciences invertebrate fossil collection before being selected for analysis. The selected specimens, which were free of siliciclastic contamination, were analyzed to assess B uptake by various invertebrate taxa and to evaluate whether skeletal B is retained or lost in fossils compared to modern specimens of the same clade. This sample suite includes unfossilized modern bioclasts (e.g., echinoids, corals, and gastropods), granular carbonate sediment (e.g., beach sands from Joulter’s Cay and Bonaire in the Caribbean, and reef sediment from Lizard Island in Australia), and carbonate fossils from sedimentary formations as old as the Ordovician. Most modern samples were collected from fully marine settings with minimal salinity variation (e.g., from ~32–33 psu in Panama to ~35–36 psu in the Caribbean; Alory et al., 2012), with a few exceptions representing brackish watermasses (e.g., ~24–28 psu in Vancouver Bay, and ~ 13–16 psu at Fort Meyers in Florida Bay; Milbrandt et al., 2016). All fossil specimens are interpreted to represent fully marine facies, although this inference cannot be conclusively demonstrated, unlike the modern samples. For context, compilations of geochemical data modern and ancient skeletal carbonate from the literature are provided in Tables S2 and S3, respectively.

2.2. Upper Cretaceous-Paleocene deep-ocean sediments

Deep-ocean sediments were obtained from drillcores at Sites 1138 A ($n = 5$), 1210B ($n = 9$), and 1258 A ($n = 10$) of the Integrated Ocean Drilling Program (IODP) (Fig. 1; Table S4). These samples were analyzed to evaluate the preservation of marine B—Ga signals over extended geological timescales (~50–100 Myr) in sedimentary formations representing unequivocally marine depositional settings. Hole 1138 A (53°33.105′S; 75°58.493′E) is located on the Kerguelen Plateau, an oceanic large igneous province (LIP) in the southern Indian Ocean that was active in the Early Cretaceous (Frey et al., 2000; Nicolaysen et al., 2000). The analyzed samples consist of argillaceous limestones spanning the lower Turonian through upper Danian. Hole 1210B (32°13.420′N; 158°15.562′E) is located on the Shatsky Rise, an oceanic LIP in the west-central Pacific that was active during the Late Jurassic to Early Cretaceous (Sager et al., 2016). The samples comprise nearly pure (i.e., non-argillaceous) limestones spanning the middle Campanian to lower Danian. Hole 1258 A (9°26.000′N; 54°43.999′W) is located on the Demerara Rise, an oceanic LIP near the coast of Surinam and French Guyana that was active in the Late Jurassic in association with the Sierra Leone Hotspot (Basile et al., 2020). The analyzed samples are non-calcareous to slightly calcareous shales spanning the middle Campanian to lower Danian.

2.3. Upper Pennsylvanian cyclothemic sediments of North American Midcontinent Sea

The North American Midcontinent Sea (NAMS) was an extensive, shallow inland sea that episodically covered much of the central United States during the Late Pennsylvanian (~310–300 Ma) (Fig. 2) (Algeo and Heckel, 2008). It was largely landlocked and connected to the global ocean via a single deepwater channel extending from the western end of the Anadarko Basin through the Panhandle Strait and Hovey Channel into the eastern Panthalassic Ocean (Algeo et al., 2008). Situated in the humid tropics, the NAMS experienced substantial freshwater runoff driven by monsoonal circulation (Tabor and Poulsen, 2008). This resulted in a strongly positive water balance that promoted the development of an extensive halocline and strong water-column stratification (Algeo et al., 2008). The region was also subjected to glacio-eustatic sea-level changes associated with the Late Paleozoic Ice Age (LPIA), which caused large sea-level fluctuations of ca. 100–150 m (Joachimski et al., 2006; Rygel et al., 2008). These fluctuations produced cyclic successions of marine and terrestrial deposits known as cyclothems (Heckel, 1986, 2008; Algeo and Heckel, 2008).

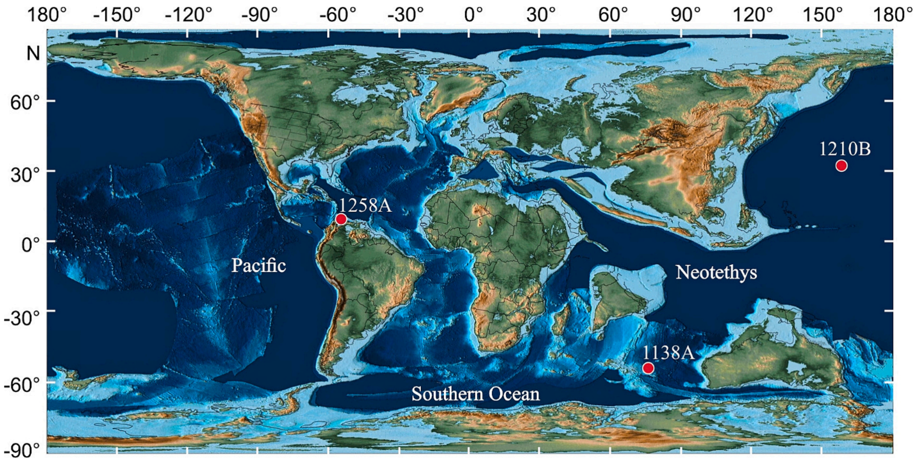

Fig. 1. Late Cretaceous (68 Ma) global paleogeography showing locations of IODP Sites 1138 A (Kerguelen Plateau), 1210B (Shatsky Rise), and 1258 A (Demerara Rise) (modified from Scotese, 2013).

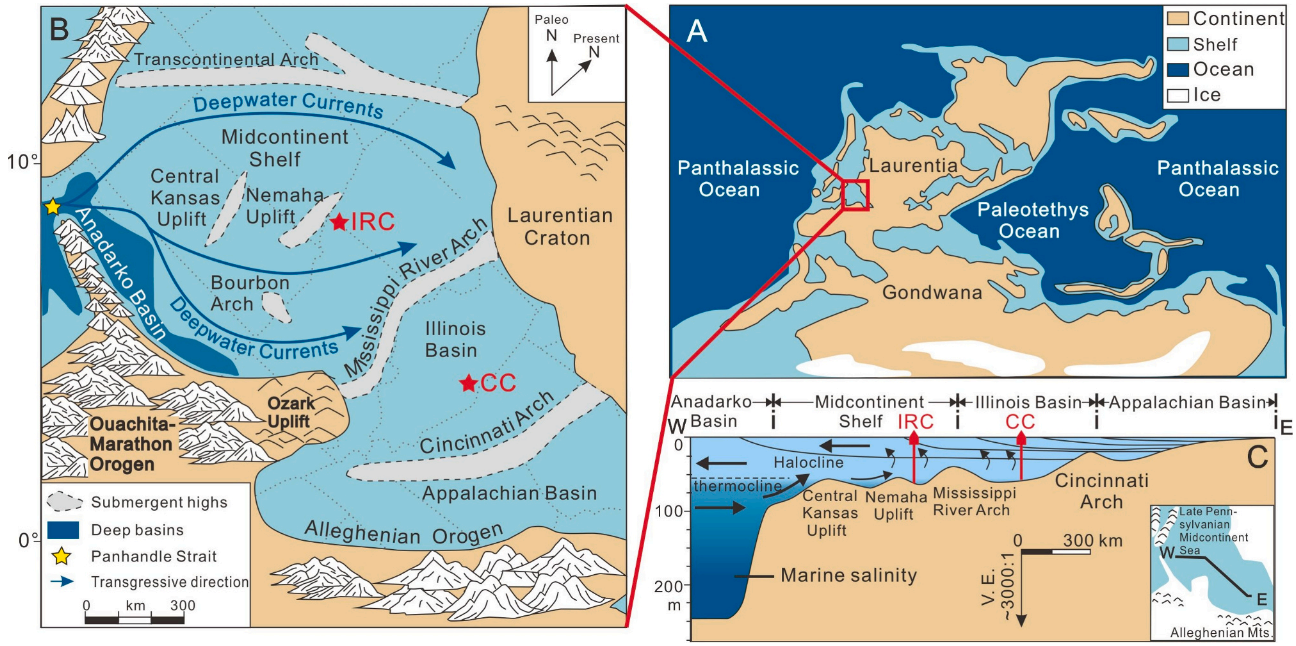

Fig. 2. Late Pennsylvanian (~305 Ma) paleogeographic maps at a glacio-eustatic highstand of the LPIA for (A) the world, (B) the North American Midcontinent Sea (NAMS), and (C) cross-section of the NAMS (from Algeo et al., 2008). Red stars mark locations of the Iowa Riverton core (IRC) and the Charleston core (CC). V.E.—vertical exaggeration. (For interpretation of the references to colour in this figure legend, the reader is referred to the web version of this article.)

The study primarily used samples from the Iowa Riverton Core (IRC) in southwestern Iowa (40.600°N, 95.575°W) (Fig. 2; Table S5). This core represents a site on the Late Pennsylvanian Midcontinent Shelf of North America that was affected by advection of open-ocean waters from the Eastern Tropical Panthalassic Ocean (Algeo and Heckel, 2008; Algeo and Herrmann, 2018). We analyzed 333 samples from a 74.3-m-thick interval spanning the upper Desmoinesian to upper Missourian stages. This includes 196 limestone and marl samples from shallow-water units of varying salinity characteristics (e.g., Amoret/Altamont, Sniabar, Bethany Falls, Winterset, Wester Valley, Cement, Paola, Raytown, Argentine, Plattsburg Captain Creek and Stoner limestone members) and 137 calcareous and non-calcareous shale samples from deep-water cyclothemic ‘core shales’ of marine or near-marine character (e.g., Eudora and Quivira shales) along with some ‘outer shales’ deposited in nearshore environments of uncertain salinity (e.g., Bonner Springs Shale) (Algeo et al., 2025). We also report data for 10 shale samples of the Stark Shale Member of the Dennis Limestone cyclothem from the Charleston Core (CC) in east-central Illinois (39.502°N, 88.218°W) (Fig. 2; Table S6). This core represents a more proximal location to the east of the Mississippi River Arch (Algeo and Herrmann, 2018) and, hence, within a more restricted region of the NAMS that was subject to greater freshwater influence. These samples were originally analyzed in a prior study (Wei et al., 2022).

2.4. *Upper Devonian limestone and shale formations of Alberta Basin*

We analyzed 31 limestone samples from the Westerdale Member and 12 shale samples from the Duvernay Fm from the Frasnian (lower Upper Devonian) Woodbend Group of the Alberta Basin (Table S7). The Alberta Basin forms part of the larger Western Canada Sedimentary Basin (WCSB) (MacKay and Pedersen, 2022; Zhang et al., 2023). During the Late Devonian, this region was situated near the equator and featured carbonate deposition on well-oxygenated shallow-marine platforms (e.g., Cooking Lake Fm) and pinnacle reefs (e.g., Leduc Limestone). These carbonates interfingered with, and were subsequently onlapped by, organic-rich shales and mixed calcareous-argillaceous lithologies deposited in mostly anoxic deep-basin environments (e.g., Duvernay and Ireton formations), all of which are assigned to the Woodbend Group (Fig. 3A; Switzer et al., 1994; Shaw and Harris, 2022). The Westerdale Member of the Lower Ireton Fm consists of <15 m of argillaceous limestone deposited during an oxic stage of basinal sedimentation. It is stratigraphically equivalent to the Upper Leduc Limestone (Glass, 1990; Mossop and Shetsen, 1994). The Duvernay Shale comprises finely laminated dark brown to black, bituminous shales and argillaceous limestones with an average thickness of ~50–100 m (Harris et al., 2018; Thorson et al., 2022). It is a major petroleum source rock (Knapp et al., 2019), deposited under deep-water, low-energy conditions. Stratigraphically, it corresponds to the Lower Leduc Limestone (Fig. 3B; Chow et al., 1995; Stasiuk and Fowler, 2004; Wang et al., 2016).

3. Methods

Major- and trace-element concentrations, including B, were analyzed using Inductively Coupled Plasma-Mass Spectrometry (ICP-MS). Prior to trace-element analysis, approximately 40 mg of sample powder were dissolved in a concentrated HF-HNO_3 mixture (15 mol/L HF and 12 mol/L HNO_3) in a high-pressure Teflon bomb. For B concentration analyses, an alkaline fusion method outlined by Cai et al. (2023) was followed. In that method, ~40 mg of sample powder were placed in a nickel crucible with hydrated Na_2O_2 and placed on a hotplate at 90 °C. After drying to a paste, the crucibles were covered and heated to ~700 °C for 10 min. After cooling, the residue was redissolved using 3 mL of 1.0 mol/L HCl and transferred into a 15 mL centrifuge tube. 3 mL of milli-Q water was added to the crucible and heated to 50 °C for 5 min to remove any alkaline cake remaining in the crucible. After transferring all of the crucible contents into the 15 mL centrifuge tube, 0.5 mL aliquots of 6.0 mol/L HCl were added and the sample vortexed until all of the hydroxide precipitate was redissolved. Both solutions were then diluted to 50 mL with 3 % HNO_3. An internal standard solution containing 10 mg/L of Rh was used to correct for signal drift. All analyses were performed at ALS Chemex in Brisbane, Australia, with analytical precisions better than ±2 % for major elements and ± 5 % for trace elements (including B).

Results were rigorously calibrated using blanks, replicate samples, and internal laboratory standards to ensure accuracy and precision as

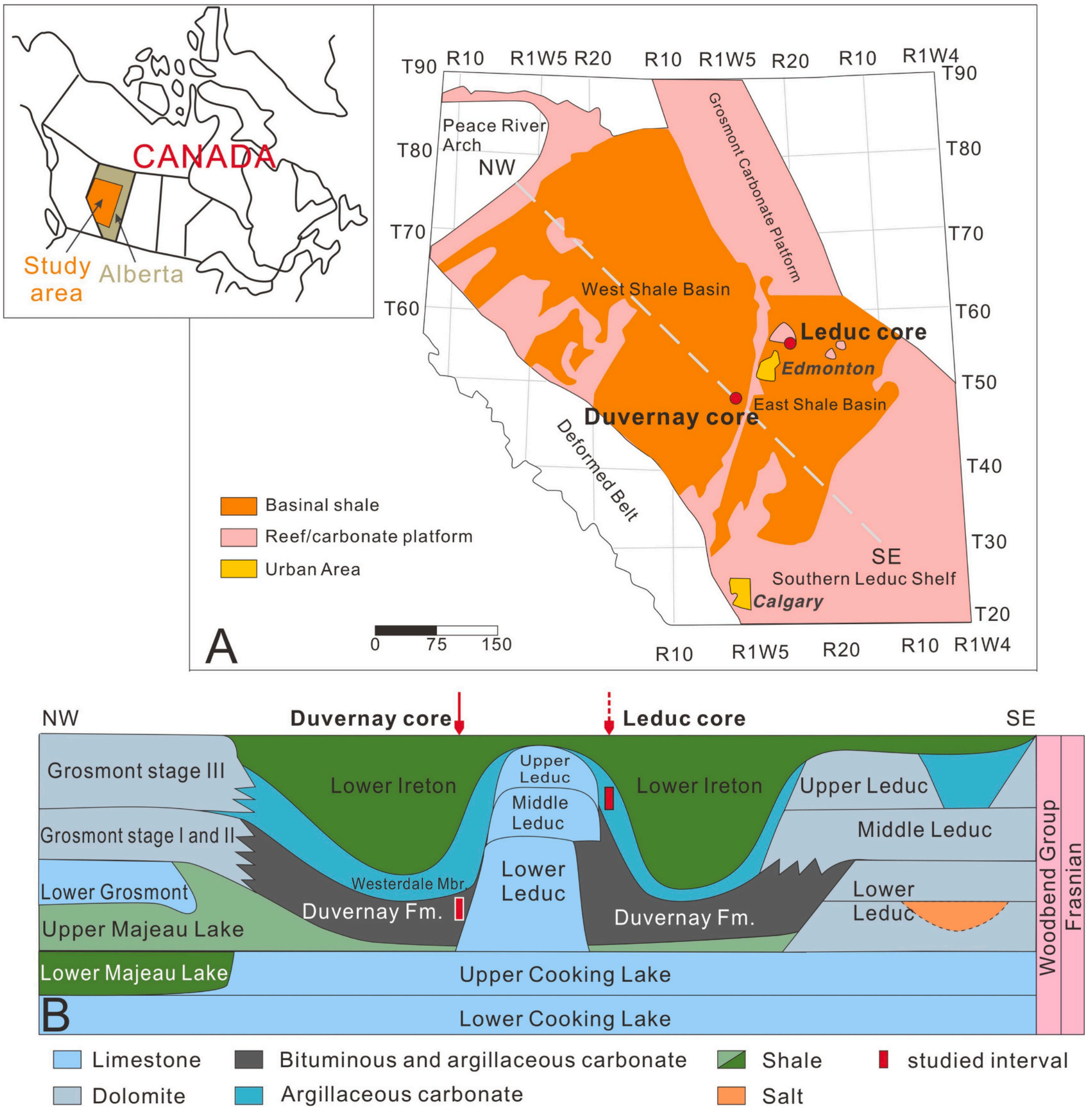

Fig. 3. (A) Locations of Westerdale Member limestone and Duvernay Shale core sites in Alberta Basin. (B) Stratigraphic cross-section of Upper Devonian units in the Alberta Basin, from NW to SE, showing approximate sampling intervals of Westerdale Member and Duvernay Shale. Note, for visualization purposes, the pinnacle reef between the East and West Shale Basins is shown as a broader feature than it actually is. Modified from Wang et al., 2016; Knapp et al., 2017; Harris et al., 2018).

follows. A blank, a replicate sample, internal laboratory standards, and an internationally recognized standard (GSR-6) were introduced into the analytical sequence at regular intervals, typically after every 6 unknowns. This systematic approach was employed to monitor and correct for any potential instrumental drift or contamination, thereby ensuring the reliability and consistency of the measured data. Results for B and Ga and given in units of parts per million (ppm), and B/Ga was calculated as a weight ratio.

4. Results and salinity interpretations

4.1. Normalization of boron concentration data

B, Ga and Al are in the same family of the periodic table, i.e., the Boron Group. Although they have similarities in some chemical properties, Ga (unlike B) is a common substituent in aluminous minerals (Yuan et al., 2021) and resides primarily in the clay-mineral fraction of siliciclastic sediments, as shown by strong positive correlations of Ga and Al in all the present suites of study samples (Fig. 4). The ubiquitous linear relationship between Ga and Al suggests that either element could be used to normalize B contents. However, Ga was selected over Al because its concentrations (~10–20 ppm) are much closer to the typical B content of shale, compared to the significantly higher concentrations of Al (~60,000–90,000 ppm) (Wei and Algeo, 2020).

4.2. Modern and ancient skeletal carbonates

A set of 45 bioclasts and skeletal sediments was analyzed for a suite of major and trace elements (Table S1). Among the 26 modern carbonate specimens, B content was highest in red algae (161 ppm; $n = 1$), with intermediate values for corals (median 79 ppm, range 65–89 ppm; $n = 6$), and bryozoans (74 ppm and 94 ppm; $n = 2$; Table S1) [note: all geochemical data are reported as medians and 16th-to-84th percentile ranges to avoid the influence of outliers]. Lower values were obtained for skeletal sands (median 45 ppm, range 36–64 ppm; $n = 6$) and mollusks (i.e., bivalves and gastropods; median 21 ppm, range 17–27 ppm;

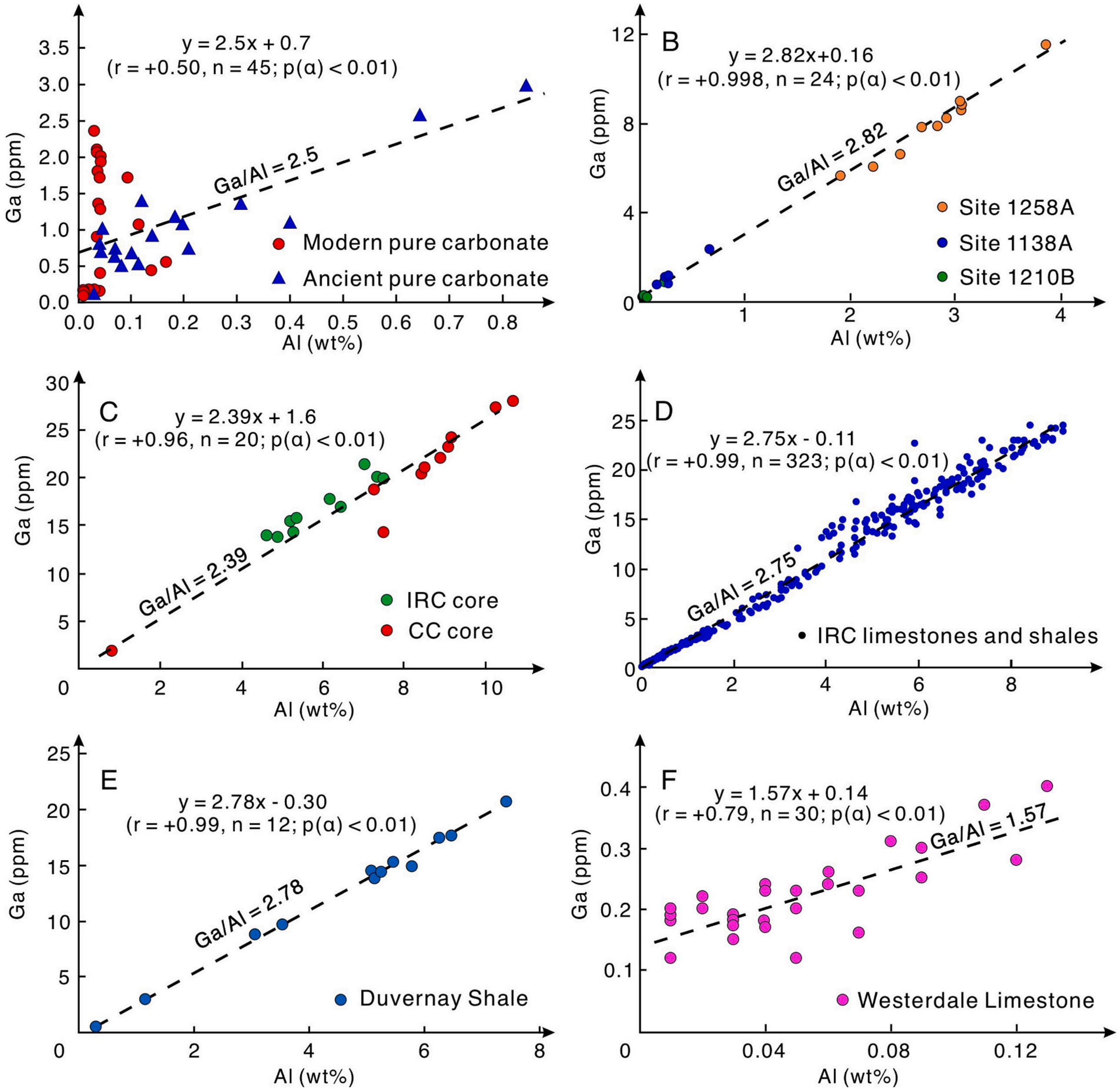

Fig. 4. Crossplots of Ga versus Al for (A) modern and ancient skeletal carbonates; (B) Cretaceous-Paleocene IODP samples; (C) Upper Pennsylvanian IRC and CC core shales; (D) IRC core limestones and shales; (E) Upper Devonian Duvernay Shale; and (F) Upper Devonian Westerdale Limestone. Pearson correlation coefficients are >0.96 except for (F), where Al concentrations are very low.

$n = 7$). These data are comparable with published B concentration data for modern corals (median 64 ppm, range 50–84 ppm; $n = 59$), surface sediments of mixed skeletal bioclasts (median 27 ppm, range 11–55 ppm; $n = 130$), and bivalves (median 9 ppm, range 3–17 ppm; $n = 4$) (Table S2). Thus, modern marine carbonate bioclasts take up substantial amounts of B from seawater—amounts that are nearly as large as those in typical marine shales (i.e., ~90–120 ppm) (Fig. 5).

Ancient skeletal samples ($n = 19$) also contain substantial B, although the amounts are consistently lower than in modern specimens of the same taxon, as observed in an Ordovician alga (28 ppm; $n = 1$), Ordovician-Devonian brachiopods (median 24 ppm, range 22–43 ppm; $n = 5$), and Ordovician-Miocene corals and bryozoans (median 16 ppm, range 15–22 ppm; $n = 7$). These data are comparable with published values for ancient carbonate bioclasts including brachiopods (median 30 ppm, range 17–47 ppm; $n = 60$), corals (median 42 ppm, range 24–50 ppm; $n = 131$), foraminifera (median 11 ppm, range 7–13 ppm; $n = 20$), and bioclastic limestone (median 4.0 ppm, range 0.8–8.0 ppm; $n = 74$) (Table S3). Thus, ancient marine bioclasts retain substantial amounts of B, although at levels typically ~30–50 % lower than for modern marine bioclasts.

For the full set of carbonate skeletal samples, B content exhibits a significant negative correlation with Ga ($r = -0.34$, $p(a) = \sim 0.02$; Fig. 6A), and Al a moderate negative correlation with Ca ($r = -0.23$, $p(a) = 0.13$; Fig. 6B). Given the status of Ga as a clay-mineral proxy (Fig. 4), these relationships indicate that B is mainly resident not in clay contaminants but, rather, in the carbonate lattices of these samples. Mn covaries negatively with Sr ($r = -0.60$, $p(a) \sim 0.03$; Fig. 6C), suggesting that Mn was gained as Sr was lost from these specimens during diagenesis, making the Mn/Sr ratio a valid proxy for degree of diagenetic alteration. However, the low [Mn] (<50 ppm), high [Sr] (>50 ppm), and low Mn/Sr ratios (<1) for nearly all the carbonate skeletal specimens are an indication that they have experienced little or no diagenetic alteration (Peral et al., 2007). The ancient bioclastic samples exhibit high Ca contents (median 33.1 %, range 30.6–38.2 %; Fig. 6A), low Al (median 0.11 %, range 0.04–0.32 %) and Ga contents (median 0.78 %, range 0.53–1.33 %; Fig. 6B), and low Mn/Sr ratios (≤1.3; Fig. 6C). These data are consistent with, at most, only minor clay contamination of the carbonate bioclasts.

Carbonate produced by algae and corals tends to incorporate more B into the mineral lattice than that of other organisms (Hemming and Hanson, 1992). This pattern is partly due to the preferential uptake of B in aragonite relative to calcite (n.b., the former mineral has larger structural sites to accommodate $B(OH)_4^-$; Lippmann, 1973), and partly due to clade-specific biomineralization processes (e.g., mollusk shells are known to acquire fewer impurities than the shells of most other invertebrate clades; Piwoni-Piórewicz et al., 2021). Both theoretical and experimental studies (Hemming and Hanson, 1992; Uchikawa et al., 2015; Kaczmarek et al., 2016) show that, rather than being a simple substitution of $HBO_{3(aq)}^{2-}$ for $CO_{3(aq)}^{2-}$ in the crystal lattice, B incorporation into carbonates is an adsorption-precipitation process, whereby negatively-charged $B(OH)_{4(aq)}^-$ ions are adsorbed onto positively-charged calcite crystal surfaces and finally coprecipitated as occlusions or inclusions during formation of new layers of calcite (Wang et al., 2018). These considerations account for the substantial, although variable, amounts of B present in modern skeletal carbonates (Fig. 5A).

Modern carbonate sediments tend to acquire higher B contents (median 44 ppm, range 17–74 ppm) than ancient carbonate sediments (median 25 ppm, range 5.3–46 ppm) (Fig. 5). The differences in B content between modern and ancient carbonates are almost certainly due to partial loss of B from the carbonate mineral lattice during diagenetic recrystallization (Paris et al., 2010). Loosely adsorbed B on carbonate mineral surfaces is even more prone to diagenetic loss (Morse, 1986). As aragonite recrystallizes more readily at an early diagenetic stage, primary aragonite grains may have a tendency to lose more B than primary calcite grains (Vengosh et al., 1991). Although direct data are lacking, it is reasonable to assume that similar proportions of B are lost from bioclasts regardless of their initial B content, which depends on the salinity conditions of their formation). Consequently, marine carbonates should generally retain higher B concentrations than brackish and freshwater carbonates even after diagenesis (Vengosh et al., 1991; Hemming and Hanson, 1992; Pagani et al., 2005). In closed (late-stage) diagenetic systems, the B released from carbonates may adsorb onto coexisting clay minerals, preventing complete loss of B from the sediment (Williams et al., 2001). These processes likely account for the substantial, though incomplete, retention of B in skeletal carbonates following diagenesis (Fig. 5B).

4.3. *Upper Cretaceous-Paleocene deep-ocean sediments*

The Cretaceous-Paleogene samples represent various lithologies yielding differing ranges of B, Ga and Al values (Table S4). Site 1210B, consisting of nearly pure limestone, exhibits the lowest B and Al but highest Ca contents, with B ranging from 8 to 18 ppm (median 9 ppm), Al from 0.03 to 0.05 % (median 0.04 %), Ca from 35.9 to 36.3 % (median 36.2 %), and B/Ga from 33 to 44 (median 35; Fig. 7A-B). Site 1138 A, consisting of argillaceous limestone, exhibits intermediate B, Ca and Al contents, with B ranging from 5 to 11 ppm (median 11 ppm), Al from 0.22 to 0.41 % (median 0.27 %), Ca from 33.6 to 35.2 % (median 34.8

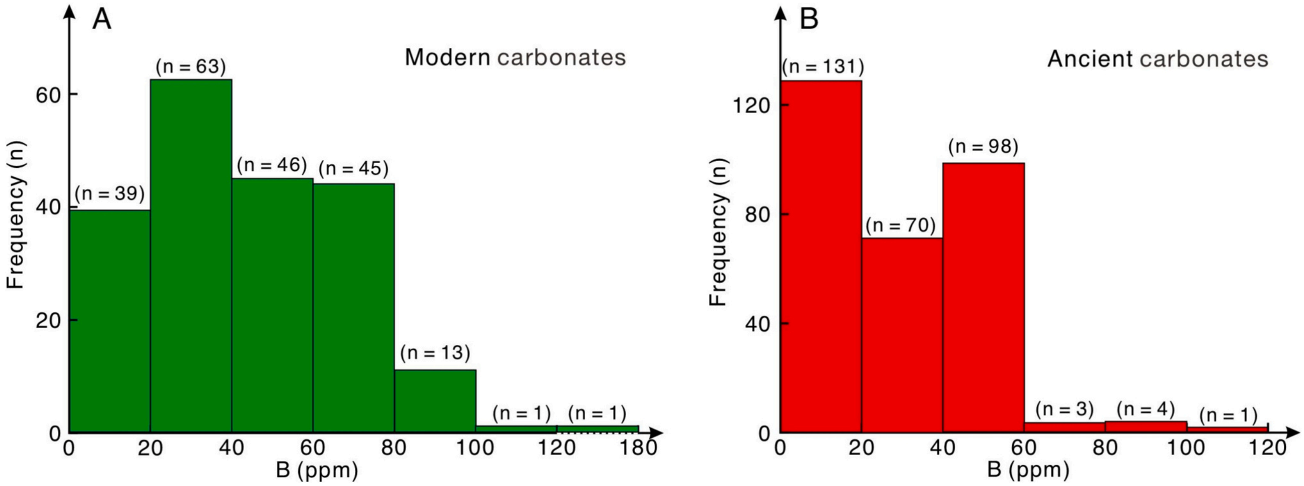

Fig. 5. Elemental B content distribution of (A) modern and (B) ancient carbonate samples. Data sources include the 45 bioclasts of the present study in Table S1, and the published studies given in Table S2 and S3.

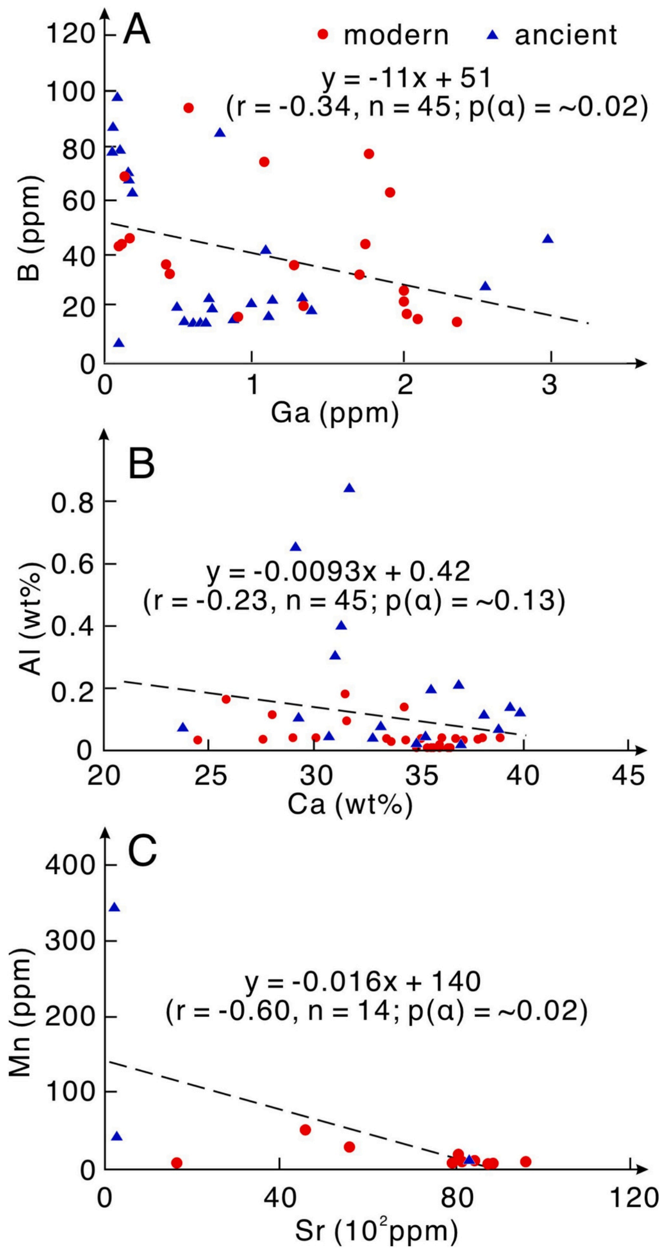

Fig. 6. Modern and ancient skeletal carbonates: (A) B vs. Ga, (B) Al vs. Ca, and (C) Mn vs. Sr. Note Mn concentrations were not analyzed for 31 of the 45 samples.

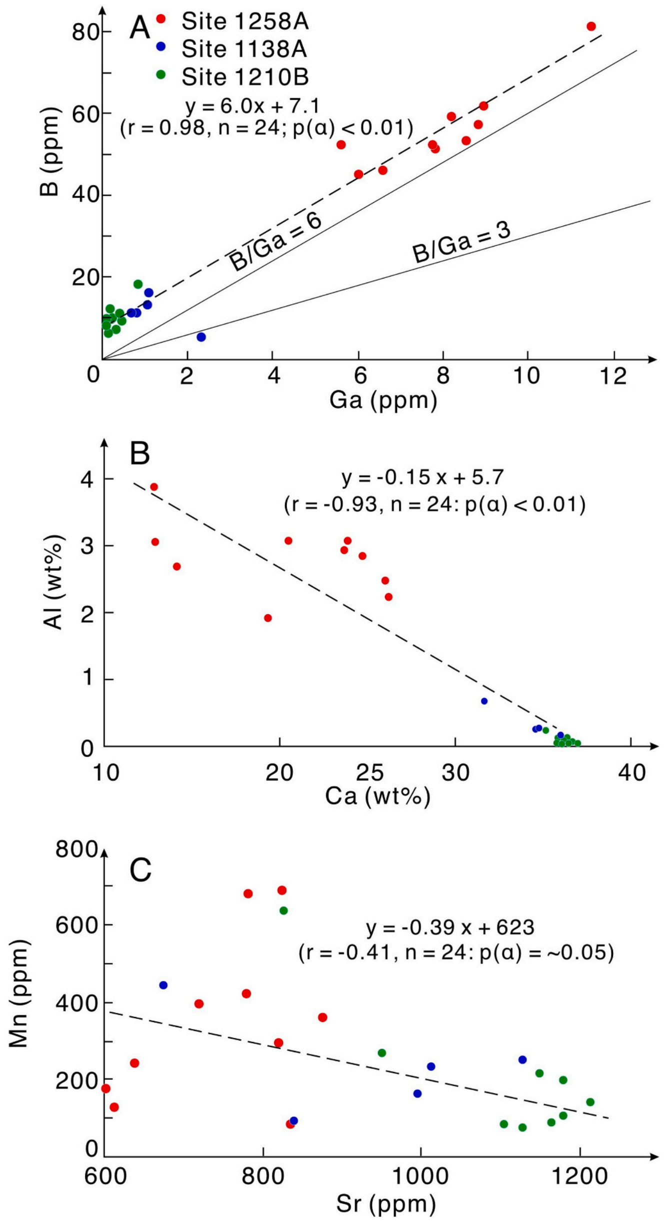

Fig. 7. (A) B vs. Ga, (B) Al vs. Ca, and (C) Mn vs. Sr for samples from IODP Sites 1138 A, 1210B, and 1258 A.

%), and B/Ga from 10.1 to 14.5 (median 13.1). Site 1258 A, consisting of shale, exhibits the highest B and Al and lowest Ca contents, with boron ranging from 45 to 81 ppm (median 52 ppm), Al from 2.3 to 3.1 % (median 2.9 %), Ca from 13.5 to 25.4 % (median 22.1 %), and B/Ga from 6.5 to 7.3 (median 6.7). The Mn/Sr ranges of Sites 1210B, 1138 A, and 1258 A are 0.07–0.25 (median 0.11), 0.14–0.38 (median 0.22), and 0.23–0.70 (median 0.39), respectively, indicating limited diagenesis at all sites (Fig. 7C).

Because these deep-ocean Cretaceous and Paleocene samples originate from environments with well-established normal-marine salinity regimes, they would be expected to yield normal-marine B/Ga ratios of 6 to 10 (Wei and Algeo, 2020; Wei et al., 2022). The shale samples (Site 1258 A) yield B/Ga ratios (6.5–7.3) exclusively within this range, confirming the preservation of marine salinity signals in ancient shale formations having experienced only marine phreatic diagenesis. In contrast, the argillaceous limestone samples from Site 1138 A exhibit slightly elevated B/Ga values (10.1–14.5), while the nearly pure limestone samples display significantly higher B/Ga values (33–44). These latter results are due to diminished Ga concentrations with increasing carbonate content, inflating the B/Ga ratio (see Section 5.1 for further discussion). Thus, B/Ga values in carbonate-rich sediments cannot be interpreted using the B/Ga salinity facies thresholds established for shales and mudstones (Wei et al., 2018; Wei and Algeo, 2020). Significantly, the full set of samples exhibits a regression running parallel to, and slightly above, the marine B/Ga threshold of 6, with a *y*-intercept of 7 ppm B and only limited variation around this regression line (ca. ±5 ppm B) (Fig. 7A). This suggests that all lithologies (shales and limestones) exhibit similar levels of B enrichment above the marine B/Ga threshold of 6, despite their compositional differences.

4.4. *Upper Pennsylvanian cyclothemic sediments of North American Midcontinent Sea*

The Upper Pennsylvanian samples are mostly from the IRC core ($n =$

333) with a small subset from the CC core ($n = 10$). Among the former, 196 are from carbonate-rich facies and 137 from shale facies; all 10 of the CC samples consist of shale. The carbonate-rich samples yielded medians (ranges) of 20 (8–48.8) for B/Ga, 0.9 % (0.2–3.1 %) for Al, and 31 % (19–37 %) for Ca, and the shale samples yielded medians (ranges) of 6.65 (5.57–7.96) for B/Ga, 6.6 % (5.1–8.1 %) for Al, and 0.7 % (0.4–1.8 %) for Ca (Fig. 8; Table S5). Whereas the shale samples exhibit a typical range of B/Ga values for epicratonic formations, the interbedded carbonate samples yield far higher values because of small Ga content denominators (cf. Section 4.3). However, as with the Cretaceous IODP samples (Fig. 7A), the full set of Pennsylvanian samples (i.e., shales and limestones) exhibits a regression running parallel to, and slightly above, the marine B/Ga threshold of 6 with a y-intercept of ~7 ppm B (Fig. 8 A). Although the variance of the smaller set of Cretaceous samples about its regression line is more limited (ca. ±5 ppm B), among the Pennsylvanian samples the degree of variance is smaller for the limestones (ca. ±10 ppm B) than for the shales (±20–30 ppm B). For both the Pennsylvanian and Cretaceous samples, this pattern demonstrates that the limestones accumulated under marine-salinity conditions (note: this inference was not in doubt for the deep-ocean Cretaceous samples, but it was uncertain for the epicratonic Pennsylvanian samples). An Al-vs-Ca crossplot shows that the Pennsylvanian samples consist mainly of two components: clay minerals and carbonate (Fig. 8B). Among the carbonate-rich samples, most show low contents of both Sr and Mn, although a small subset shows modest Mn enrichment, reflecting minor carbonate diagenesis (Fig. 8C).

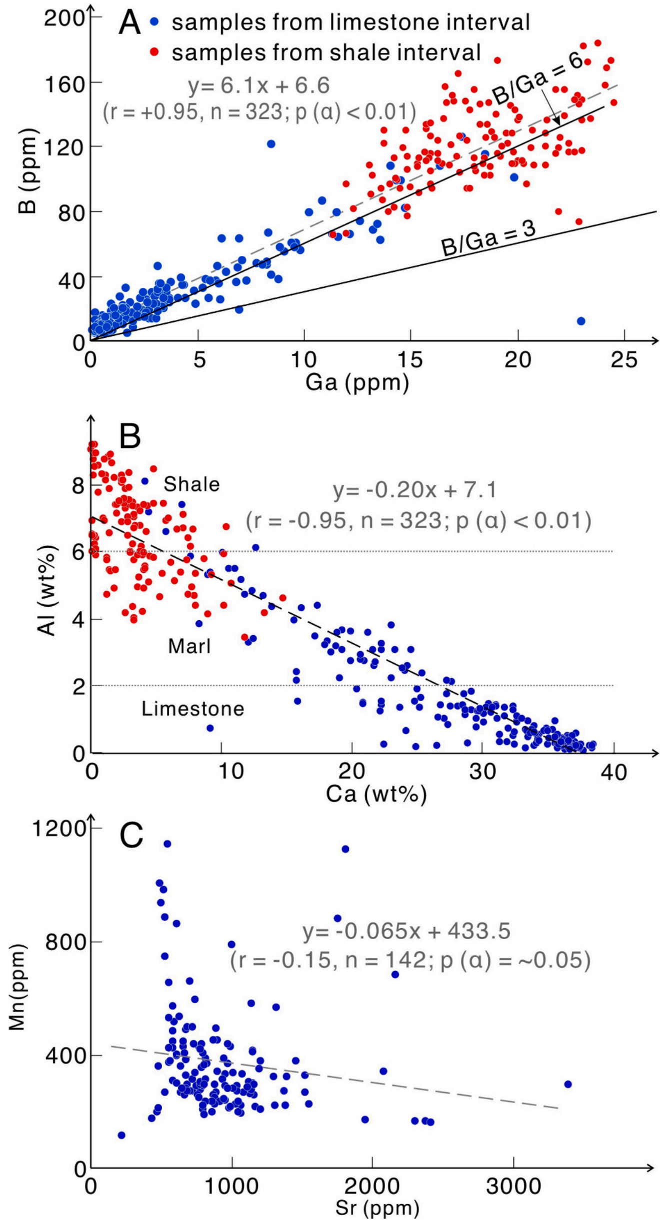

Fig. 8. B versus (A) Ga, (B) Al, and (C) Ca of Upper Pennsylvanian samples from IRC core, North American Midcontinent Sea. Blue and red dots represent samples collected from carbonate-rich and shale-rich intervals, respectively. In panel C, only limestone samples with Al < 2 % were plotted because the Mn/Sr ratio is a tool for evaluation of diagenesis in carbonate sediments (Brand and Veizer, 1980). (For interpretation of the references to color in this figure legend, the reader is referred to the web version of this article.)

4.5. *Upper Devonian formations of Alberta Basin, western Canada*

The Westerdale Limestone and Duvernay Shale, although not strictly correlative, were deposited together within the Alberta Basin, a semi-restricted epicratonic basin in western Canada, during the early Frasnian Stage of the Late Devonian, likely within a fairly short time interval (probably <1 Myr). There is no evidence to suggest significant changes in watermass characteristics of the basin during this period. However, the two units may have been deposited under different salinities as a function of water depth: the Westerdale Ls accumulated in the surface layer and the Duvernay Shale in the deep layer. If a vertical salinity gradient existed, the surface waters associated with the Westerdale Limestone would have experienced lower salinities compared to the deeper waters in which the Duvernay Shale accumulated. Salinity and density stratification have been documented in other Late Devonian basins of North America (e.g., Algeo et al., 2007, Algeo et al., 2008; Gilleaudeau et al., 2021, 2023; Song et al., 2021; Remírez et al., 2025), suggesting that watermass stratification may have existed within the Late Devonian Alberta Basin.

The Westerdale Limestone yields B, Al and Ca contents of 5–14 ppm (median 7 ppm), 0.01–0.13 % (median 0.04 %), and 36.6–37.6 % (median 37.2 %), respectively (Fig. 9; Table S7). In contrast, the Duvernay Shale shows broader ranges for these elements: 15–178 ppm (median 146 ppm) for B, 0.31–7.43 % (median 5.20 %) for Al, and 8.0–26.6 % (median 12.7 %) for Ca. B shows a significant positive correlation with Ga (Fig. 9 A, D) and Al (not shown) for both units, and a negative correlation with Ca for the Duvernay Shale (Fig. 9B; n.b., the B—Ca correlation is non-significant for the Westerdale Ls owing to a small range of Ca concentrations; Fig. 9E). These relationships demonstrate that uptake of aqueous B is more effective in siliciclastic facies than in carbonate facies. Both units exhibit low ranges of Mn/Sr ratios (median 0.16, range 0.14–0.22 for the Westerdale; median 0.84, range 0.61–0.93 for the Duvernay), indicating limited diagenetic effects (Fig. 9C, F). The Westerdale Ls is a nearly pure limestone with minimal siliciclastic contamination, whereas the Duvernay Shale displays a spectrum of compositions ranging from weakly to strongly calcareous, with the more carbonate-rich samples being marls or, for two samples with Ca > 30 %, black limestones. These lithological differences account for the much wider ranges of geochemical variation observed in the Duvernay Shale compared to the Westerdale Ls.

The B/Ga ratios of the Westerdale and Duvernay formations are 22–75 (median 33) and 8.6–36 (median 10.4), respectively. The less-calcareous Duvernay samples (i.e., Ca < 20 %; $n = 9$) yield B/Ga ratios (~8–13) that are consistent with normal marine to slightly hypersaline watermass salinities. The B/Ga ratios of these samples are always modestly higher than those of equivalent lithologies from other formations in this study, as seen in a crossplot of B/Ga versus Al (Fig. 10). This pattern suggests that the deep waters of the Late Devonian Alberta Basin had above-normal marine salinities, i.e., that they were slightly hypersaline. This inference is consistent with the subtropical paleolatitude (20–25°S) of the study area during the Frasnian (Domeier and Torsvik, 2014; Hauck, 2014), which would have promoted evaporation of surface

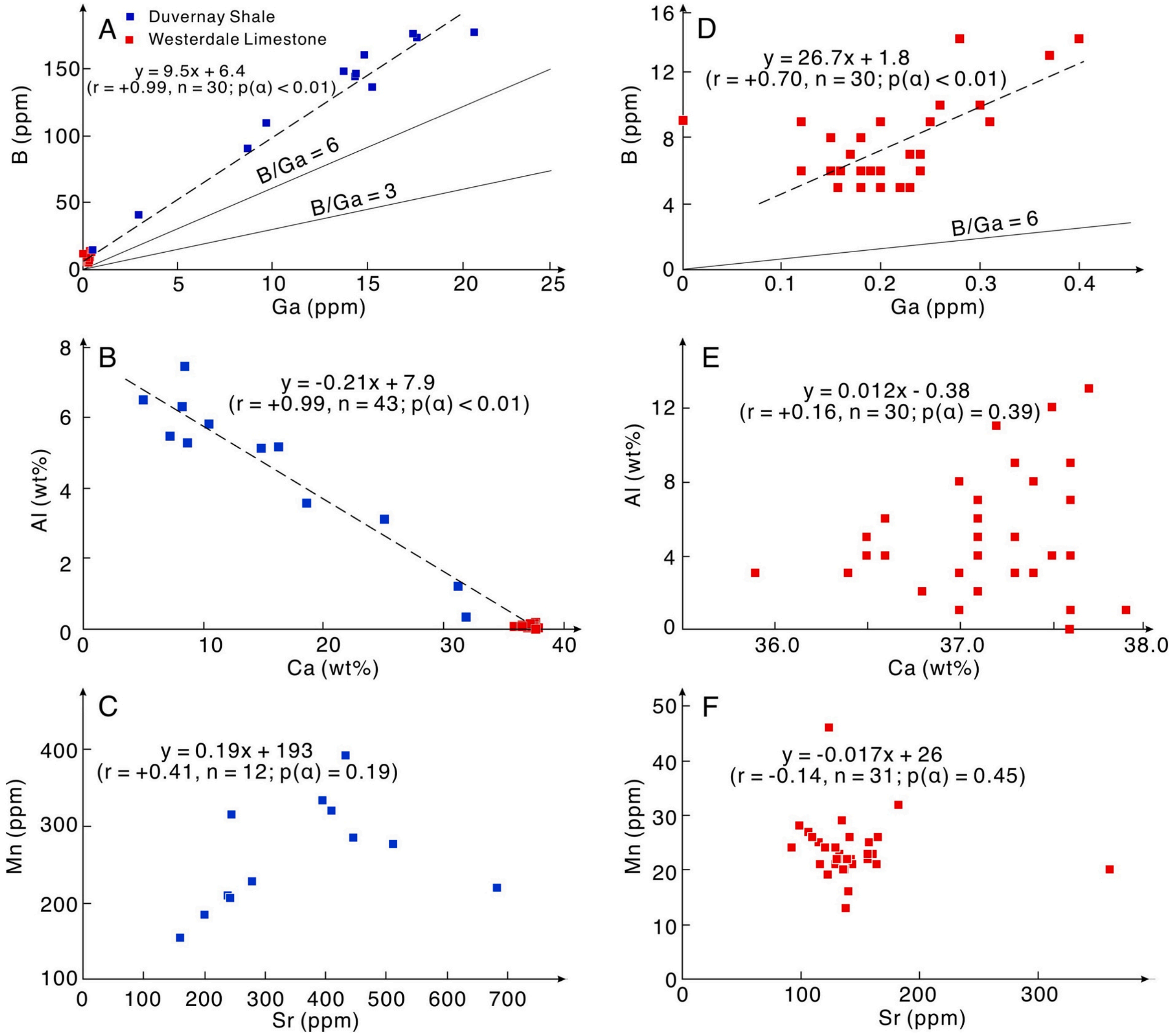

Fig. 9. (A, D) B versus Ga; (B, E) B versus Al; and (C, F) B versus Ca for the Devonian Westerdale Limestone and Duvernay Shale.

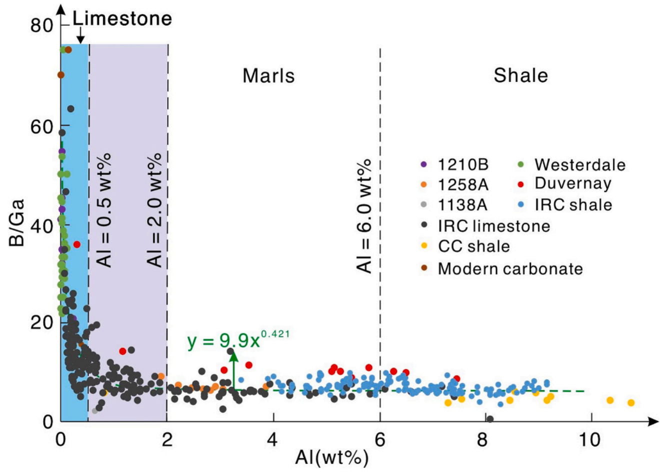

Fig. 10. B/Ga versus Al for all samples analyzed in the present study. Rising B/Ga values below Al of ~2 % are due to small denominator size (i.e., low Ga content) and the presence of a small fraction of total B that is not hosted by clay minerals. The B/Ga proxy is generally a robust estimator of salinity for samples with >2.0 % Al, and sometimes reliable for samples with 0.5–2.0 % Al, but it is unreliable for samples with <0.5 % Al.

waters. In the arid subtropical climate belt, evaporation on shallow platforms can densify watermasses that subsequently flow over the platform margin and sink into adjacent basinal areas (cf. Friedrich et al., 2008; Roveri et al., 2014).

The Westerdale Ls and the more-calcareous Duvernay samples (i.e., Ca > 20 %, $n = 3$) have significantly higher B/Ga ratios (>15), which, as with the limestones of the Cretaceous and Pennsylvanian sample suites, are almost certainly artifacts of low Ga concentrations (see Section 5.1). The regression of B versus Ga for the Devonian sample suite has a slope of 9.5, which is significantly greater than the marine B/Ga threshold of 6, and a y-intercept of ~6 ppm B (Fig. 9 A), which is essentially identical to that of the Cretaceous and Pennsylvanian sample suites. These relationships support the interpretation that the Westerdale Ls accumulated under marine salinity conditions, whereas the Duvernay Shale formed under slightly hypersaline conditions.

5. Discussion

5.1. Uptake of boron in carbonate and marly sediments

The primary mechanism for the removal of B from the water column into sediments is adsorption onto clay minerals (Goldberg et al., 1993; Wei and Algeo, 2020). This is true not only for shales but also for most limestones and marls, as evidenced by the ubiquitous positive correlation between B with Ga (and Al) contents (Figs. 7A, 8 A, 9 A) and the negative correlation of B with Ca content (Figs. 7B, 8B, 9C). These relationships confirm that B is dominantly taken up by clay minerals, regardless of the sedimentary environment. In contrast, clean carbonates, such as modern and ancient skeletal carbonates, show no positive relationship between B and Ga (or Al) content (Fig. 6A), reflecting the absence or minimal presence of clay minerals. An important implication of these observations is that as long as a sufficient quantity of clay minerals are present in a sample, its B/Ga ratio can reliably indicate the salinity of the watermass in which it accumulated.

This raises a key question: what constitutes "a sufficient quantity" of clay minerals to effectively record the ambient B/Ga salinity signal of a watermass? We addressed this by plotting B/Ga versus Al (a proxy for clay-mineral content) across all study samples, which mainly represent marine facies with small sample subsets from weakly brackish and weakly hypersaline facies (Fig. 10). The results show essentially invariant B/Ga values between ~5 and ~ 10 for all samples with Al content >2 %. This pattern suggests that the B/Ga proxy is a robust estimator of depositional salinity for shales (Al > 6 %) and marls (Al = 2–6 %). However, the data distribution shows that B/Ga values begin to rise systematically for samples with Al < 2 %, although only modestly over the Al range of 0.5–2 % but then sharply for Al < 0.5 % (Fig. 10). Considering the strong positive correlation between Al and Ga in nearly all formations ($r > +0.96$; Fig. 4), this trend indicates that the rise in B/Ga ratios with declining Al (i.e., clay-mineral) content is a function of diminishing Ga concentrations. Low Ga content leads to unstable normalizations of B concentrations, resulting in artificially elevated B/Ga ratios in clay-poor samples.

Although our analyses have demonstrated that B predominantly resides in the clay-mineral fraction of sediments (Figs. 7A, 8 A, 9 A), the sharp increase in B/Ga ratios with diminishing clay-mineral content (Fig. 10) suggests that a small fraction of total B is hosted by non-clay phases. This fraction might represent B taken up into the lattice of carbonate minerals (Wang et al., 2018; Kobayashi et al., 2020), B adsorbed onto the surfaces of carbonate minerals (Hemming and Hanson, 1992; Ruiz-Agudo et al., 2012), or B associated with organic material (Niaz et al., 2007; Bolan et al., 2023). While this non-clay B fraction is essentially negligible in clay-rich sediments (i.e., Al > 2 %), it becomes proportionally larger, and eventually dominant, as clay content decreases (i.e., Al ➔ 0 %). Based on these findings, we infer that the B/Ga salinity proxy can be used confidently in sediments with >2 % Al but should not be used in samples with <2 % Al.

It is well established that factors such as pH and redox conditions significantly influence the adsorption of B onto clay minerals (Vengosh et al., 1991; Kuliński et al., 2017). In seawater, B primarily exists as $B(OH)_3$ and $B(OH)_4^-$, with their relative abundances being pH-dependent (You et al., 1995). Clay minerals exhibit a strong affinity for $B(OH)_4^-$, resulting in significant B adsorption under weakly alkaline pH conditions, such as seawater. In contrast, clay-mineral affinity for $B(OH)_3$ is weaker, leading to reduced B adsorption in low-pH environments typical of many freshwater systems (Vengosh et al., 1991). Additionally, B concentrations are inversely correlated with dissolved oxygen levels, with anoxic waters generally exhibiting higher concentrations of B than oxic waters (Bennett, 2017; Kuliński et al., 2017). Notably, pH and redox conditions often covary with salinity, particularly in coastal and marine environments, both in modern and ancient systems (Millero, 2007; Gattuso et al., 2011; Gilleaudeau et al., 2021). Given this interplay of factors, we propose that, despite the influence of pH and redox conditions, variations in the B/Ga ratio recorded in the clay-mineral fraction of carbonate-rich sediments can serve as a reliable semi-quantitative proxy for changes in watermass salinity.

5.2. Excess boron as a salinity proxy in carbonate-rich samples

All of the ancient formations analyzed in this study were deposited in watermasses of marine or near-marine salinity, with only minor variations towards weakly brackish (some Pennsylvanian samples) to weakly hypersaline conditions (some Devonian samples). All of the shale and marl formations (#3, 5, 7 in Table 1) exhibit B/Ga ratios consistent with marine salinity, whereas all of the limestone formations (#1, 2, 4, 6 in Table 1) exhibit abnormally high B/Ga ratios due to low Ga concentrations. Thus, the B/Ga proxy is not valid for paleosalinity analysis of samples containing less than 2 % Al. However, many low-Al samples in the study formations align with the B versus Ga trends indicative of marine salinity conditions (Figs. 7A, 8 A, 9 A). This suggests that paleosalinity signals are preserved in these samples but are obscured by the influence of low Ga concentrations. Therefore, a methodological approach is needed to recover and reliably interpret the paleosalinity signals in such low-Ga (i.e., carbonate-rich) samples.

We propose a new proxy called "excess boron" (B_{xs}) for this purpose. Excess boron is defined as the amount of B above a minimum threshold signifying normal-marine salinity conditions (Fig. 11). It is calculated as:

$$B_{xs} = B_{total} - Ga \times (B/Ga)_{marine} \tag{1}$$

where $(B/Ga)_{marine}$ is equal to 6, i.e., the threshold value for the marine salinity facies (Wei and Algeo, 2020).

A test of the three sets of ancient formations examined in this study shows that limestone and shale facies generally yield similar levels of B_{xs} (typically 5 to 15 ppm), demonstrating the potential robustness of B_{xs} as a salinity proxy for carbonate facies. For the Cretaceous deep-ocean sample suite, similar amounts of B_{xs} are present in each of the three sections, regardless of lithologic differences: 6.6–9.9 ppm (median 7.7 ppm) at Site 1210B, 6.2–8.0 ppm (median 6.6 ppm) at Site 1138 A, and 3.8–10.6 ppm (median 6.3 ppm) at Site 1258 A (Fig. 11B; Table 1). The same pattern is observed for the Pennsylvanian limestones (1.7–11.1 ppm, median 5.9 ppm), although the Pennsylvanian shale samples yield slightly lower B_{xs} values (−8.2 ppm to 13.6 ppm, median 1.2 ppm; Fig. 11C; Table 1), which is consistent with deposition of some of these shales in deltaic systems (Algeo et al., 2025). The Devonian study units are an exception, as the shales yield far higher B_{xs} values (35.5 to 69.5 ppm, median 56.8 ppm) than the limestones (4.7 to 8.2 ppm, median 5.6 ppm) (Fig. 11D; Table 1).

The B_{xs} data for the Westerdale Ls and Duvernay Shale offer potentially valuable insights into the salinity structure of the Late Devonian Alberta Basin. The median B_{xs} value of the Westerdale Ls (5.6 ppm) is similar to those of the unambiguously marine Cretaceous units, both limestones and shales (6.3–7.7 ppm) as well as that of the mostly marine Pennsylvanian limestones (5.9 ppm) (Table 1). This correspondence supports the interpretation that these units record typical marine salinity conditions. In contrast, the Duvernay Shale records strongly elevated B_{xs} (56.8 ppm) and moderately elevated B/Ga values (10.4), suggesting deposition under slightly hypersaline conditions. These data imply that the Late Devonian Alberta Basin had a salinity-stratified watermass, with marine surface waters and hypersaline deep waters. This salinity stratification may have resulted from its subtropical location (20–25°S; Domeier and Torsvik, 2014), allowing evaporation of surface waters on nearby shallow shelves (Fowler et al., 2001), or possibly from dissolution of subsurface evaporites within the basin (Zidane et al., 2014). The former explanation (i.e., surface evaporation) seems more likely given the slight degree of salinity enrichment of the deep watermass because stratified oceanic watermasses in which the deep layer is hypersaline due to evaporite dissolution commonly have highly elevated salinities (to 100 s of psu), as in the modern Orca Basin (Tribovillard et al., 2008).

We examined the relationship between the B/Ga and B_{xs} proxies for all of the samples of the present study (Fig. 12). The samples were categorized by clay content (as proxied by Al), with Al concentrations of <0.5 %, 0.5–2 %, and > 2 % representing clean limestone, argillaceous limestone, and marls plus shales, respectively. For marls and shales, the relationship of B_{xs} to B/Ga ratio is nearly perfect ($r = +0.95$) because both proxies are based on B and Ga concentrations, and both B and Ga

Table 1
Statistics of elemental proxy distributions for sample suites of the present study.

#	Location	Formation	B/Ga	B (ppm)	Ga (ppm)	Al (%)	B_{xs} (ppm)
1	Shatsky Rise IODP Site 1210B	Cret. deep-ocean limestone	34.8 32.7–44.4	9.0 8.0–11.2	0.23 0.21–0.26	0.04 0.03–0.05	7.7 6.6–9.9
2	Kerguelen Plateau IODP Site 1138 A	Cret. deep-ocean argillaceous ls.	13.1 8.5–14.6	11.0 8.9–14.1	1.1 0.80–1. 6	0.27 0.22–0.41	6.6 6.2–8.0
3	Demerara Rise Site IODP Site 1258 A	Cret. deep-ocean shale	6.8 6.5–7.3	52.5 48.2–59.6	8.0 6.3–8.9	2.9 2.3–3.1	6.3 3.8–10.6
4	IRC N. Am. Midcontinent Sea	Penn. limestone (Al < 2 wt%)	11.0 6.8–18.7	14.5 7.0–26	1.3 0.5–3.2	0.51 0.19–1.3	5.9 1.7–11.1
5	IRC N. Am. Midcontinent Sea	Penn. shale & marl (Al > 2 wt%)	6.2 5.1–7.5	58.0 36.5–84.1	8.7 6.1–13.9	3.3 2.5–5.4	1.2 −8.2 to 13.6
6	Alberta Basin, western Canada	Up. Devon. Westerdale Ls.	33.3 28.6–44.6	7.7 6.0–9.4	0.20 0.16–0.27	0.04 0.02–0.08	5.6 4.7–8.2
7	Alberta Basin, western Canada	Up. Devon. Duvernay Shale	10.4 9.7–12.1	146 79–175	14.3 7.2–17.4	5.2 2.6–6.3	56.8 35.5–69.5

Note: In each table cell, the upper value represents the median (50th percentile) of the distribution, and the lower values are the 16th-to-84th percentile range.

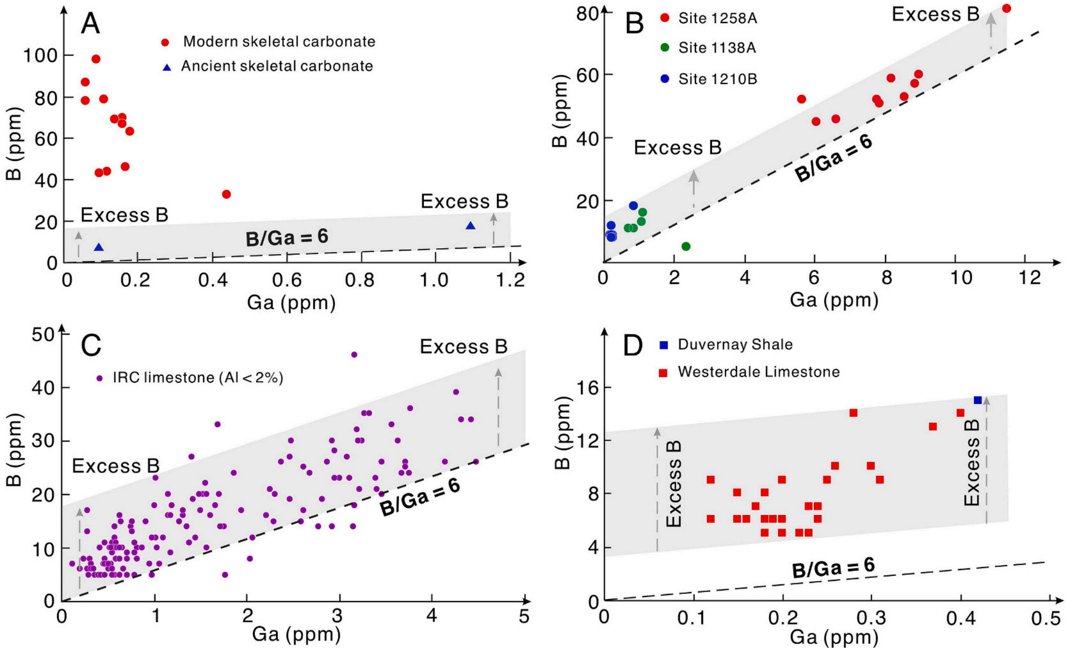

Fig. 11. Crossplots of B versus Ga, showing excess boron (B_{xs}) values for **(A)** modern and ancient skeletal carbonates; **(B)** Upper Cretaceous-Paleocene limestone and shale samples; **(C)** Upper Pennsylvanian limestone samples (Al < 2 %); and **(D)** Upper Devonian limestone samples. The gray fields represent the approximate range of excess B values for each formation.

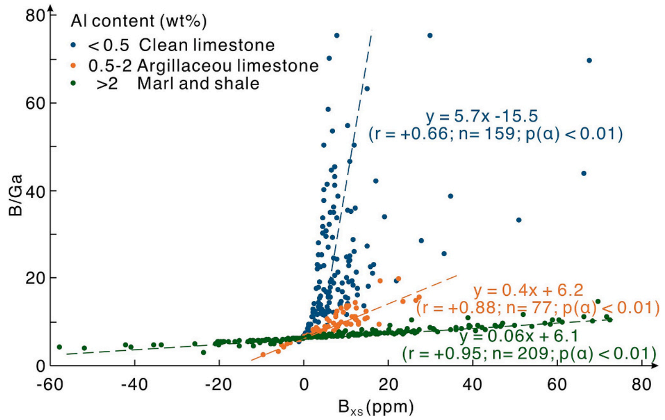

Fig. 12. Crossplot of B/Ga versus B_{xs} for all samples of the present study. Samples are categorized by clay content, as proxied by Al concentration.

concentration measurements are robust for these lithologies. The relationship breaks down for argillaceous limestones and clean limestones because Ga concentration measurements are no longer robust (often <1 ppm, which is close to or below the instrumental detection limit), generating large variability in the denominator of the B/Ga ratio. The excess B proxy removes Ga as a denominator, eliminating variability introduced by low Ga concentrations. For marls and shales, the B_{xs} proxy is redundant, i.e., it provides exactly the same information as the B/Ga proxy. However, for limestones, B_{xs} provides a superior estimate of salinity than B/Ga (Fig. 12).

5.3. *Comparison with other salinity proxies for carbonate facies*

A final consideration is how the proposed B_{xs} proxy compares to other salinity proxies that have previously been developed for or applied to carbonate sediments. Proposed salinity proxies for limestone and marl facies are mostly based on isotopic compositions or elemental ratios in either bulk carbonate or specific types of skeletal carbonate (e.g., $\delta^{18}O$, Mg/Ca and Sr/Ca, $\delta^{2}H$) (Pretet et al., 2014; He et al., 2016; Lettéron et al., 2017; Vetter et al., 2017; Groeneveld et al., 2018). Carbonate $\delta^{18}O$ is controlled by the temperature and isotopic composition of the precipitating fluid and species-dependent “vital effects” (LeGrande and Schmidt, 2011). The Mg/Ca ratio of foraminiferal calcite is an important proxy for estimating past ocean temperatures. Used in conjunction with $\delta^{18}O$ of foraminiferal calcite it allows deconvolution of temperature and ice-volume signals to infer past ocean temperatures and salinities (Ferguson et al., 2008). When integrated with Mg/Ca in calcite (for temperature correction; Ferguson et al., 2008; Schmidt et al., 2004; Stott et al., 2004) and Sr/Ca in aragonite (Gillikin et al., 2005), $\delta^{18}O$ can be used to reconstruct past ocean conditions like temperatures, freshwater input and global ice volume. This method provides a paleosalinity estimate with an approximate uncertainty of ±5 psu (Rohling and Bigg, 1998; Dämmer et al., 2020; Jöhnck et al., 2021). Another independent approach to paleosalinity reconstruction leverages the relationship between compound-specific $\delta^{2}H$ (= δD) of marine algal biomarkers and surface seawater salinity, with an approximate uncertainty of ±7 psu (Dämmer et al., 2020; Jöhnck et al., 2021; Jia et al., 2022).

The application of geochemical proxies for watermass salinity in carbonate facies is limited by several factors. For example, salinity estimates based on $\delta^{18}O$-Mg/Ca analysis are influenced by additional variables affecting aqueous oxygen isotopic composition, such as hydrological changes, glacial-interglacial variation in continental ice volume, and sea-level fluctuations. Moreover, theses analyses require specific fossil carriers for the signal, with $\delta^{18}O$-Mg/Ca analysis primarily applied to foraminifera and Sr/Ca analysis to corals and sclerosponges (Gillikin et al., 2005; LeGrande and Schmidt, 2011). Diagenetic processes, such as dissolution and recrystallization, commonly modify the oxygen isotopic and elemental compositions of skeletal carbonates, compromising the robustness of salinity estimates based on older fossils (Gillikin et al., 2005; LeGrande and Schmidt, 2011; Geske et al., 2012). Similarly, the burial degradation of the organic matter presents a significant challenge in applying $\delta^{2}H$ as a salinity proxy for marine algae (He et al., 2016; Liu et al., 2018). As a consequence, these considerations confine the utility of these proxies to well-preserved fossils and younger geologic intervals, such as the Quaternary Period. Although these proxies may offer slightly higher precision in salinity estimates (ca. ±10 psu) compared to the elemental proxies B/Ga and B_{xs}, their utility is restricted to specific fossil taxa and well-preserved carbonate shells with geologically young sedimentary units. In contrast, B-based proxies, including B/Ga and Bxs, are more versatile. They can be applied to bulk carbonate sediments across a much broader range of ages, making them valuable for studying ancient depositional systems where fossil preservation is poor or specific taxa are unavailable.

6. Conclusions

Testing the B/Ga salinity proxy across a range of lithologies - including shales, marls, and limestones – has confirmed its broad applicability to marine and marine-influenced facies with Al contents as low as 2 % (i.e., all shales and marls). However, in argillaceous limestones (with 0.5–2.0 % Al content), B/Ga values tend to be slightly elevated relative to the actual salinity conditions of deposition, reflecting the influence of reduced but still significant clay content. Clean limestones (with <0.5 % Al content) yield highly unreliable salinity estimates using the B/Ga proxy, owing to excessively small and variable denominators linked to low clay content. To address these limitations, we propose a new proxy for evaluating the salinity characteristics of skeletal carbonates and bioclastic carbonate sediments: “excess boron” (B_{xs}). This proxy is calculated as: $B_{total} - 6 \times Ga$, where 6 represents the minimum B/Ga threshold for marine salinity facies. In this study, marine limestones of various ages (sub-Recent, Cretaceous, and Devonian) yielded B_{xs} values of ~5–20 ppm, with a regression intercept of ~7–8 ppm B for each formation. Conversely, limestones deposited under brackish conditions tend to yield B_{xs} values <0 ppm. Thus, B_{xs} shows significant promise for extending salinity analysis to ancient limestone formations, particularly where conventional proxies struggle due to diagenetic alteration or low clay content. Its application could provide valuable insights into the depositional environments of carbonate-rich systems throughout Earth history.

CRediT authorship contribution statement

Wei Wei: Writing – review & editing, Writing – original draft, Formal analysis, Data curation, Conceptualization. **Thomas J. Algeo:** Writing – review & editing, Conceptualization. **David Meyer:** Resources. **Jiangsi Liu:** Writing – review & editing. **Katherine N. Snihur:** Formal analysis, Data curation. **Cody Lazowski:** Writing – review & editing, Formal analysis, Data curation. **Zhiquan Li:** Writing – review & editing. **Daniel S. Alessi:** Writing – review & editing. **Kurt O. Konhauser:** Writing – review & editing, Conceptualization. **Yuansheng Du:** Writing – review & editing, Conceptualization. **Wenchao Yu:** Writing – review & editing, Conceptualization.

Declaration of competing interest

All authors: Wei Wei, Thomas J. Algeo, David Meyer, Jiangsi Liu, Katherine N. Snihur, Cody Lazowski, Zhiquan Li, Daniel S. Alessi, Kurt O. Konhauser , Yuansheng Du, Wenchao Yu confirm that there are no known conflicts of interest associated with this publication and there has been no significant financial support for this work that could have influenced its outcome.

Acknowledgments

We thank the Integrated Ocean Drilling Program (College Station, Texas) for providing Cretaceous samples, the Kansas and Illinois geological surveys for providing Pennsylvanian samples, and the Canadian Geological Survey for providing Devonian samples. We thank Lan and Haley Wei for providing bivalves specimens collected from Vancouver. This research was funded by National Science and Technology Major Project (2022YFF0800200), China Geological Survey Major Project (12120114046601), National Science Foundation of China (41202086, 41472122, and 41302089), and China Scholarship Council (CSC). The project was supported by the “CUG Scholar” Scientific Research Funds at China University of Geosciences (Wuhan) (Project No. 2022153).

Appendix A. Supplementary data

Supplementary data to this article can be found online at https://doi.org/10.1016/j.chemgeo.2025.122751.

Data availability

Data will be made available on request.

References

Algeo, T.J., Heckel, P.H., 2008. The late Pennsylvanian Midcontinent Sea of North America: a review. Palaeogeogr. Palaeoclimatol. Palaeoecol. 268 (3–4), 205–221.

Algeo, T.J., Herrmann, A.D., 2018. An ancient estuarine-circulation nutrient trap: the late Pennsylvanian Midcontinent Sea of North America. Geology 46 (2), 143–146.

Algeo, T.J., Heckel, P.H., Maynard, J.B., Blakey, R., Rowe, H., 2008. Modern and ancient epeiric seas and the super-estuarine circulation model of marine anoxia. In: Pratt, B. R., Holmden, C. (Eds.), Dynamics of Epeiric Seas: Sedimentological, Paleontological and Geochemical Perspectives. Geological Association of Canada, pp. 7–38. Special Publication 48.

Algeo, T.J., Lyons, T.W., Blakey, R.C., Over, D.J., 2007. Hydrographic conditions of the Devono–Carboniferous North American Seaway inferred from sedimentary Mo–TOC relationships. Palaeogeogr. Palaeoclimatol. Palaeoecol. 256 (3–4), 204–230.

Algeo, T.J., Wei, W., Sweet, D.E., 2025. Salinity variation in Carboniferous cyclothemic successions. Chem. Geol. (in press).

Alory, G., Maes, C., Delcroix, T., Reul, N., Illig, S., 2012. Seasonal dynamics of sea surface salinity off Panama: The far Eastern Pacific Fresh Pool. J. Geophys. Res. Oceans. 117 (4), 13.

Basile, C., Girault, I., Paquette, J.L., Agranier, A., Loncke, L., Heuret, A., Poetisi, E., 2020. The Jurassic magmatism of the Demerara Plateau (offshore French Guiana) as a remnant of the Sierra Leone hotspot during the Atlantic rifting. Sci. Rep. 10 (1), 7486.

Bennett, G.L., 2017. Status and Understanding of Groundwater Quality in the North San Francisco Bay Shallow Aquifer study unit, 2012; California GAMA Priority Basin Project (ver. 1.1; Feb. 2018). U.S. Geological Survey, Washington, D.C., p. 88. Rept. 2017–5051.

Boggs, S., 2006. Principles of Sedimentology and Stratigraphy. Pearson Prentice Hall, Upper Saddle River, New Jersey, p. 608.

Bolan, S., Wijesekara, H., Amarasiri, D., Zhang, T., Ragályi, P., Brdar-Jokanović, M., Rékási, M., Lin, J.Y., Padhye, L., Zhao, H., Wang, L., Rinklebe, J., Wang, H., Siddique, H.M., Kirkham, M.B., Bolan, N., 2023. Boron contamination and its risk management in terrestrial and aquatic environmental settings. Sci. Total Environ. 894, 164744.

Brand, U., Veizer, J., 1980. Chemical diagenesis of a multicomponent carbonate system; 1, Trace elements. J. Sediment. Res. 50 (4), 1219–1236.

Cai, Y., Ruan, T., Li, Y., Li, B., Zhang, W., Li, Z., Wei, H., Rasbury, E.T., 2023. Improved alkaline fusion method for B isotope and concentration measurements of silicate materials. J. Anal. At. Spectrom. 38 (10), 1934–1942.

Cheng, M., Zhang, Z., Algeo, T.J., Liu, S., Liu, X., Wang, H., Chang, B., Jin, C., Pan, W., Cao, M., Li, C., 2021. Hydrological controls on marine chemistry in the Cryogenian Nanhua Basin (South China). Earth Sci. Rev. 218, 103678.

Cheng, M., Zhang, Z., Jin, C., Wei, W., Wang, H., Algeo, T.J., Li, C., 2023. Salinity variation and hydrographic dynamics in the early Cambrian Nanhua Basin (South China). Sci. China Earth Sci. 66 (6), 1268–1278.

Chow, N., Wendte, J., Stasiuk, L.D., 1995. Productivity versus preservation controls on two organic-rich carbonate facies in the Devonian of Alberta: Sedimentological and organic petrological evidence. Bull. Can. Petrol. Geol. 43, 433e460.

Dämmer, L.K., de Nooijer, L., van Sebille, E., Haak, J.G., Reichart, G.J., 2020. Evaluation of oxygen isotopes and trace elements in planktonic foraminifera from the Mediterranean Sea as recorders of seawater oxygen isotopes and salinity. Clim. Past 16 (6), 2401–2414.

Domeier, M., Torsvik, T.H., 2014. Plate tectonics in the late Paleozoic. Geosci. Front. 5 (3), 303–350.

Ferguson, J.E., Henderson, G.M., Kucera, M., Rickaby, R.E.M., 2008. Systematic change of foraminiferal Mg/ca ratios across a strong salinity gradient. Earth Planet. Sci. Lett. 265 (1–2), 153–166.

Fowler, M.G., Stasiuk, L.D., Hearn, M., Obermajer, M., 2001. Devonian hydrocarbon source rocks and their derived oils in the Western Canada Sedimentary Basin. Bull. Can. Petrol. Geol. 49 (1), 117–148.

Frey, F.A., et al., 2000. Origin and evolution of a submarine large igneous province: the Kerguelen Plateau and Broken Ridge, southern Indian Ocean. Earth Planet. Sci. Lett. 176 (1), 73–89.

Friedrich, O., Erbacher, J., Moriya, K., Wilson, P.A., Kuhnert, H., 2008. Warm saline intermediate waters in the cretaceous tropical Atlantic Ocean. Nat. Geosci. 1 (7), 453–457.

Gattuso, J.P., Bijma, J., Gehlen, M., Riebesell, U., Turley, C., 2011. Ocean acidification: knowns, unknowns, and perspectives. Ocean Acidific. 291–311.

Geske, A., Zorlu, J., Richter, D.K., Buhl, D., Niedermayr, A., Immenhauser, A., 2012. Impact of diagenesis and low-grade metamorphosis on isotope (δ^{26}Mg, δ^{13}C, δ^{18}O and ^{87}Sr/^{86}Sr) and elemental (Ca, Mg, Mn, Fe and Sr) signatures of Triassic sabkha dolomites. Chem. Geol. 332, 45–64.

Gilleaudeau, G.J., Algeo, T.J., Lyons, T.W., Bates, S., Anbar, A.D., 2021. Novel watermass reconstruction in the early Mississippian Appalachian Seaway based on integrated proxy records of redox and salinity. Earth Planet. Sci. Lett. 558, 116746.

Gilleaudeau, G.J., Wei, W., Remírez, M.N., Song, Y., Lyons, T.W., Bates, S., Anbar, A.D., Algeo, T.J., 2023. Geochemical and hydrographic evolution of the late Devonian Appalachian Seaway: linking sedimentation, redox, and salinity across time and space. Geochem. Geophys. Geosyst. 24 (8), e2023GC010973.

Gillikin, D.P., Lorrain, A., Navez, J., Taylor, J.W., André, L., Keppens, E., Baeyens, W., Dehairs, F., 2005. Strong biological controls on Sr/ca ratios in aragonitic marine bivalve shells. Geochem. Geophys. Geosyst. 6 (5).

Glass, D.J., 1990. Lexicon of Canadian Stratigraphy, 4. Canadian Society of Petroleum Geologists, Western Canada, p. 772.

Goldberg, S., Forster, H.S., Heick, E.L., 1993. Boron adsorption mechanisms on oxides, clay minerals, and soils inferred from ionic strength effects. Soil Sci. Soc. Am. J. 57 (3), 704–708.

Groeneveld, J., Filipsson, H.L., Austin, W.E., Darling, K., McCarthy, D., Quintana Krupinski, N.B., Bird, C., Schweizer, M., 2018. Assessing proxy signatures of temperature, salinity, and hypoxia in the Baltic Sea through foraminifera-based geochemistry and faunal assemblages. J. Micropalaeontol. 37 (2), 403–429.

Harris, N.B., McMillan, J.M., Knapp, L.J., Mastalerz, M., 2018. Organic matter accumulation in the Upper Devonian Duvernay Formation, Western Canada Sedimentary Basin, from sequence stratigraphic analysis and geochemical proxies. Sediment. Geol. 376, 185–203.

Hauck, T.E., 2014. Regional Correlation of the Beaverhill Lake Group in the Subsurface of Alberta, Townships 29 to 113 and Ranges 1W4 to 13W6; Alberta Energy Regulator, AER/AGS Open File Report 2014-05, p. 29.

He, D., Anderson, W.T., Jaffé, R., 2016. Compound specific δD and δ^{13}C analyses as a tool for the assessment of hydrological change in a subtropical wetland. Aquat. Sci. 78, 809–822.

Heckel, P.H., 1986. Sea-level curve for Pennsylvanian eustatic marine transgressive-regressive depositional cycles along midcontinent outcrop belt, North America. Geology 14 (4), 330–334.

Heckel, P.H., 2008. Pennsylvanian cyclothems in Midcontinent North America as far-field effects of waxing and waning of Gondwana ice sheets. In: Fielding, C.R., Frank, T.D., Isbell, J.L. (Eds.), Resolving the Late Paleozoic Ice Age in Time and Space: Geological Society of America Special Paper 441, pp. 275–289.

Hemming, N.G., Hanson, G.N., 1992. Boron isotopic composition and concentration in modern marine carbonates. Geochim. Cosmochim. Acta 56 (1), 537–543.

Jia, J., He, J., Wei, B., Jia, G., Li, L., 2022. Relationship between compound-specific δD of marine algae biomarkers and surface seawater salinity and its implication for paleoceanography reconstruction. Adv. Earth Science 37 (4), 392.

Joachimski, M.M., von Bitter, P.H., Buggisch, W., 2006. Constraints on Pennsylvanian glacioeustatic sea-level changes using oxygen isotopes of conodont apatite. Geology 34 (4), 277–280.

Jöhnck, J., Holbourn, A., Kuhnt, W., Andersen, N., 2021. Oxygen isotope offsets in deep-water benthic foraminifera. J. Foraminifer. Res. 51 (3), 225–244.

Kaczmarek, K., Nehrke, G., Misra, S., Bijma, J., Elderfield, H., 2016. Investigating the effects of growth rate and temperature on the B/ca ratio and δ^{11}B during inorganic calcite formation. Chem. Geol. 421, 81–92.

Knapp, L.J., McMillan, J.M., Harris, N.B., 2017. A depositional model for organic-rich Duvernay Formation mudstones. Sediment. Geol. 347, 160–182.

Knapp, L.J., Harris, N.B., McMillan, J.M., 2019. A sequence stratigraphic model for the organic-rich Upper Devonian Duvernay Formation, Alberta, Canada. Sediment. Geol. 387, 152–181.

Kobayashi, K., Hashimoto, Y., Wang, S.L., 2020. Boron incorporation into precipitated calcium carbonates affected by aqueous pH and boron concentration. J. Hazard. Mater. 383, 121183.

Kuliński, K., Schneider, B., Szymczycha, B., Stokowski, M., 2017. Structure and functioning of the acid–base system in the Baltic Sea. Earth Syst. Dyn. 8 (4), 1107–1120.

LeGrande, A.N., Schmidt, G.A., 2011. Water isotopologues as a quantitative paleosalinity proxy. Paleoceanography 26 (3), 1–10.

Lettéron, A., Fournier, F., Hamon, Y., Villier, L., Margerel, J.P., Bouche, A., Feist, M., Joseph, P., 2017. Multi-proxy paleoenvironmental reconstruction of saline lake carbonates: Paleoclimatic and paleogeographic implications (Priabonian-Rupelian, Issirac Basin, SE France). Sediment. Geol. 358, 97–120.

Lippmann, F., 1973. Crystal Chemistry of Sedimentary Carbonate Minerals. Springer, Berlin, p. 96.

Liu, H., Yang, H., Cao, Y., Liu, W., 2018. Compound-specific δD and its hydrological and environmental implication in the lakes on the Tibetan Plateau. Sci. China Earth Sci. 61, 765–777.

Liu, Z.H., Algeo, T.J., Arefifard, S., Wei, W., Brett, C., Landing, E., Lev, S.M., 2024a. Testing the salinity of Cambrian to Silurian epicratonic seas. J. Geol. Soc. Lond. 181 (3), jgs2023-217.

Liu, Z.H., Algeo, T.J., Brocks, J.J., van Maldegem, L.M., Gilleaudeau, G.J., Kah, L.C., Cheng, M., Yu, W., 2024b. Salinity reconstruction in Proterozoic depositional systems. GSA Bull. 136.

MacKay, P., Pedersen, P.K., 2022. The Western Canada Sedimentary Basin: a confluence of science, technology, and ideas. AAPG Bull. 106 (3), 655–676.

Milbrandt, E.C., Bartleson, R.D., Martignette, A.J., Siwicke, J., Thompson, M., 2016. Evaluating light attenuation and low salinity in the lower Caloosahatchee Estuary with the River, Estuary, and Coastal Observing Network (RECON). Fla. sci. 109–124.

Millero, F.J., 2007. The marine inorganic carbon cycle. Chem. Rev. 107 (2), 308–341.

Morse, J.W., 1986. The surface chemistry of calcium carbonate minerals in natural waters: an overview. Mar. Chem. 20 (1), 91–112.

Mossop, G.D., Shetsen, I., 1994. Geological Atlas of the Western Canada Sedimentary Basin. Canadian Society of Petroleum Geologists and Alberta Research Council. https://ags.aer.ca/reports/atlas-western-canada-sedimentary-basin, 5 Nov. 2024.

Niaz, A., Ranjha, A.M., Rahmatullah, A.H., Waqas, M., 2007. Boron status of soils as affected by different soil characteristics–pH, $CaCO_3$, organic matter and clay contents. Pak. J. Agric. Sci. 44 (3), 428–435.

Nicolaysen, K., Frey, F.A., Hodges, K.V., Weis, D., Giret, A., 2000. ^{40}Ar/^{39}Ar geochronology of flood basalts from the Kerguelen Archipelago, southern Indian Ocean: implications for Cenozoic eruption rates of the Kerguelen plume. Earth Planet. Sci. Lett. 174 (3–4), 313–328.

Pagani, M., Lemarchand, D., Spivack, A., Gaillardet, J., 2005. A critical evaluation of the boron isotope-pH proxy: the accuracy of ancient ocean pH estimates. Geochim. Cosmochim. Acta 69 (4), 953–961.

Paris, G., Bartolini, A., Donnadieu, Y., Beaumont, V., Gaillardet, J., 2010. Investigating boron isotopes in a middle Jurassic micritic sequence: primary vs. diagenetic signal. Chem. Geol. 275 (3–4), 117–126.

Peral, L.E. G., Poiré, D.G., Strauss, H., Zimmermann, U., 2007. Chemostratigraphy and diagenetic constraints on Neoproterozoic carbonate successions from the Sierras Bayas Group, Tandilia System, Argentina. Chem. Geol. 237 (1–2), 109–128.

Piwoni-Piórewicz, A., Strekopytov, S., Humphreys-Williams, E., Kukliński, P., 2021. The patterns of elemental concentration (Ca, Na, Sr, Mg, Mn, Ba, Cu, Pb, V, Y, U and Cd) in shells of invertebrates representing different CaCO 3 polymorphs: a case study from the brackish Gulf of Gdańsk (the Baltic Sea). Biogeosciences 18 (2), 707–728.

Pretet, C., Reynaud, S., Ferrier-Pages, C., Gattuso, J.P., Kamber, B.S., Samankassou, E., 2014. Effect of salinity on the skeletal chemistry of cultured scleractinian zooxanthellate corals: Cd/ca ratio as a potential proxy for salinity reconstruction. Coral Reefs 33, 169–180.

Remírez, M.N., Algeo, T.J., 2020. Paleosalinity determination in ancient epicontinental seas: a case study of the T-OAE in the Cleveland Basin (UK). Earth Sci. Rev. 201, 103072.

Remírez, M.N., Algeo, T.J., Shen, J., Liu, J., Gilleaudeau, G.J., Zhou, L., 2024. Low-salinity conditions in the “marine” late Triassic-early Jurassic Neuquén Basin of

Argentina: challenges in paleosalinity interpretation. Palaeogeogr. Palaeoclimatol. Palaeoecol. 646, 112216.

Remírez, M.N., Gilleaudeau, G.J., Elrick, M., Putri, T., Gill, B., Algeo, T.J., 2025. Hydrographic Architecture of the Late Devonian Illinois Basin, North America. In review.

Rimstidt, J.D., Balog, A., Webb, J., 1998. Distribution of trace elements between carbonate minerals and aqueous solutions. Geochim. Cosmochim. Acta 62 (11), 1851–1863.

Rohling, E.J., Bigg, G.R., 1998. Paleosalinity and δ18O: a critical assessment. J. Geophys. Res. Oceans 103 (C1), 1307–1318.

Roveri, M., Manzi, V., Bergamasco, A., Falcieri, F.M., Gennari, R., Lugli, S., Schreiber, B. C., 2014. Dense shelf water cascading and Messinian canyons: a new scenario for the Mediterranean salinity crisis. Am. J. Sci. 314 (3), 751–784.

Ruiz-Agudo, E., Putnis, C.V., Kowacz, M., Ortega-Huertas, M., Putnis, A., 2012. Boron incorporation into calcite during growth: Implications for the use of boron in carbonates as a pH proxy. Earth Planet. Sci. Lett. 345, 9–17.

Rygel, M.C., Fielding, C.R., Frank, T.D., Birgenheier, L.P., 2008. The magnitude of late Paleozoic glacioeustatic fluctuations: a synthesis. J. Sediment. Res. 78 (8), 500–511.

Sager, W.W., Sano, T., Geldmacher, J., 2016. Formation and evolution of Shatsky rise oceanic plateau: Insights from IODP Expedition 324 and recent geophysical cruises. Earth Sci. Rev. 159, 306–336.

Schmidt, M.W., Spero, H.J., Lea, D.W., 2004. Links between salinity variation in the Caribbean and North Atlantic thermohaline circulation. Nature 428 (6979), 160–163.

Scotese, C.R., 2013. Map Folio 17, Late Cretaceous (Maastrichtian, 68 ma), PALEOMAP PaleoAtlas for ArcGIS, Volume 2, Cretaceous Paleogeographic, Paleoclimatic and Plate Tectonic Reconstructions. PALEOMAP Project, Evanston, IL.

Shaw, D.J., Harris, N.B., 2022. Facies and systems tracts at high-resolution in an organic-rich mudstone: the Duvernay Formation, Kaybob area, Alberta, Canada. Sediment. Geol. 436, 106157.

Smrzka, D., Zwicker, J., Bach, W., Feng, D., Himmler, T., Chen, D., Peckmann, J., 2019. The behavior of trace elements in seawater, sedimentary pore water, and their incorporation into carbonate minerals: a review. Facies 65, 1–47.

Song, Y., Gilleaudeau, G.J., Algeo, T.J., Over, D.J., Lyons, T.W., Anbar, A.D., Xie, S., 2021. Biomarker evidence of algal-microbial community changes linked to redox and salinity variation, Upper Devonian Chattanooga Shale (Tennessee, USA). GSA Bull. 133 (1–2), 409–424.

Stasiuk, L.D., Fowler, M.G., 2004. Organic facies in Devonian and Mississippian strata of Western Canada Sedimentary Basin; relation to kerogen type. Bull. Can. Petrol. Geol. 52 (3), 234e256.

Stott, L., Cannariato, K., Thunell, R., Haug, G.H., Koutavas, A., Lund, S., 2004. Decline of surface temperature and salinity in the western tropical Pacific Ocean in the Holocene epoch. Nature 431 (7004), 56–59.

Switzer, S.B., Holland, W.G., Christie, D.S., Graf, G.C., Hedinger, A.S., McAuley, R.J., Wierzbicki, R.A., Packard, J.J., Mossop, G.D., Shetsen, I., 1994. The Woodbend-Winterburn strata of the Western Canada Sedimentary Basin. In: Mossop, G.D., Shetsen, I. (Eds.), *Geological Atlas of the Western Canada Sedimentary Basin, 4*. Geological Survey of Canada, pp. 165–202.

Tabor, N.J., Poulsen, C.J., 2008. Palaeoclimate across the Late Pennsylvanian–Early Permian tropical palaeolatitudes: a review of climate indicators, their distribution, and relation to palaeophysiographic climate factors. Palaeogeogr. Palaeoclimatol. Palaeoecol. 268 (3–4), 293–310.

Thorson, A.M., Rau, E.G., Atchley, S.C., Yeates, D.W., 2022. Controls on East Shale Basin reservoir distribution within the Upper Devonian Duvernay Formation, Western Canada Sedimentary Basin. Mountain Geol. 59 (4), 295–314.

Tribovillard, N., Bout-Roumazeilles, V., Algeo, T., Lyons, T.W., Sionneau, T., Montero-Serrano, J.C., Riboulleau, A., Baudin, F., 2008. Paleodepositional conditions in the Orca Basin as inferred from organic matter and trace metal contents. Mar. Geol. 254 (1–2), 62–72.

Uchikawa, J., Penman, D.E., Zachos, J.C., Zeebe, R.E., 2015. Experimental evidence for kinetic effects on B/ca in synthetic calcite: implications for potential $B(OH)_4^-$ and $B(OH)_3$ incorporation. Geochim. Cosmochim. Acta 150, 171–191.

Vengosh, A., Kolodny, Y., Starinsky, A., Chivas, A.R., McCulloch, M.T., 1991. Coprecipitation and isotopic fractionation of boron in modern biogenic carbonates. Geochim. Cosmochim. Acta 55 (10), 2901–2910.

Vetter, L., Spero, H.J., Eggins, S.M., Williams, C., Flower, B.P., 2017. Oxygen isotope geochemistry of Laurentide ice-sheet meltwater across termination I. Quat. Sci. Rev. 178, 102–117.

Wang, P., Chen, Z., Pang, X., Hu, K., Sun, M., Chen, X., 2016. Revised models for determining TOC in shale play: example from Devonian Duvernay shale, Western Canada sedimentary basin. Mar. Pet. Geol. 70, 304–319.

Wang, Y.J., Wei, H.Z., Jiang, S.Y., van de Ven, T.G., Ling, B.P., Li, Y.C., Lin, Y.B., Guo, Q., 2018. Mechanism of boron incorporation into calcites and associated isotope fractionation in a steady-state carbonate-seawater system. Appl. Geochem. 98, 221–236.

Wang, X., Zhan, C., Algeo, T.J., Shen, J., Liu, Z.H., 2024. Watermass architecture of the Ordovician–Silurian Yangtze Sea (South China) and its palaeogeographical implications. J. Geol. Soc. Lond. 181 (4), jgs2023-024.

Wei, W., Algeo, T.J., 2020. Elemental proxies for paleosalinity analysis of ancient shales and mudrocks. Geochim. Cosmochim. Acta 287, 341–366.

Wei, W., Algeo, T.J., Lu, Y., Liu, H., Zhang, S., Peng, L., Zhang, J., Chen, L., 2018. Identifying marine incursions into the Paleogene Bohai Bay Basin lake system in northeastern China. Int. J. Coal Geol. 200, 1–17.

Wei, W., Yu, W., Algeo, T.J., Herrmann, A.D., Zhou, L., Liu, J., Wang, Q., Du, Y., 2022. Boron proxies record paleosalinity variation in the north American Midcontinent Sea in response to Carboniferous glacio-eustasy. Geology 50 (5), 537–541.

Wei, W., Yu, W., Du, Y., Algeo, T.J., Li, Z., Cheng, M., Wang, P., Zhang, J., Robbins, L.J., Konhauser, K., 2024. A new salinity-based model for Cryogenian Mn-carbonate deposits. Precambrian Res. 403, 107309.

Williams, L.B., Hervig, R.L., Holloway, J.R., Hutcheon, I., 2001. Boron isotope geochemistry during diagenesis. Part I. Experimental determination of fractionation during illitization of smectite. Geochim. Cosmochim. Acta 65 (11), 1769–1782.

Xia, L., Cao, J., Stüeken, E.E., Zhi, D., Wang, T., Li, W., 2020. Unsynchronized evolution of salinity and pH of a Permian alkaline lake influenced by hydrothermal fluids: a multi-proxy geochemical study. Chem. Geol. 541, 119581.

You, C.F., Spivack, A.J., Gieskes, J.M., Rosenbauer, R., Bischoff, J.L., 1995. Experimental study of boron geochemistry: implications for fluid processes in subduction zones. Geochim. Cosmochim. Acta 59, 2435–2442.

Yu, W., Algeo, T.J., Zhou, Q., Wei, W., Yang, M., Li, F., Du, Y., Pan, W., Wang, P., 2022. Evaluation of alkalinity sources to Cryogenian cap carbonates, and implications for cap carbonate formation models. Glob. Planet. Chang. 217, 103949.

Yuan, W., Chen, J., Teng, H., Chetelat, B., Cai, H., Liu, J., Wang, Z., Bouchez, J., Moynier, F., Gaillardet, J., Schott, J., Liu, C., 2021. A review on the elemental and isotopic geochemistry of gallium. Glob. Biogeochem. Cycles 35 (9), e2021GB007033.

Zhang, C., Gu, Y.J., Dokht, R.M., Chen, Y., 2023. Recovery of the Alberta Basin sedimentary structures in southern-central Alberta using nonlinear inversions of receiver functions. J. Geophys. Res. Solid Earth 128 (3), e2022JB024813.

Zidane, A., Zechner, E., Huggenberger, P., Younes, A., 2014. On the effects of subsurface parameters on evaporite dissolution (Switzerland). J. Contam. Hydrol. 160, 42–52.